ATLAS Paper Draft

HDBS-2019-08

Version 0.5

Target journal: JHEP

Comments are due by: Comments deadline

Supporting internal notes

Support note: https://cds.cern.ch/record/2788797

Paper draft: https://cds.cern.ch/record/2858627

Search for heavy resonances in final states with four leptons and missing transverse momentum or jets in pp collisions at $\sqrt{s} = 13$ TeV with the ATLAS detector

A search for a new heavy boson produced via gluon-fusion in the four-lepton channel with missing transverse momentum or jets is performed. The search uses proton–proton collision data equivalent to an integrated luminosity of 139 fb^{-1} at a centre-of-mass energy of 13 TeV collected by the ATLAS detector between 2015 and 2018 at the Large Hadron Collider. This study explores the decays of heavy bosons: $R \to SH$ and $A \to ZH$. In these processes, $S \to \text{invisible}$ and $H \to ZZ$. The Z boson associated with the heavy Higgs H decays into two leptons, jets, or invisible particles. The mass range of the heavy boson studied is 390–1300 (320–1300) GeV for the R (A) boson and 220–1000 GeV for the H boson. The mass of the S boson is set to a fixed value of 160 GeV. No significant deviation from the Standard Model backgrounds is observed. The results are interpreted as upper limits at a 95% confidence level on the $\sigma(gg \to R) \times \mathcal{B}(R \to SH) \times \mathcal{B}(H \to ZZ) \times \mathcal{B}(ZZ \to 4\ell)$ and $\sigma(gg \to A) \times \mathcal{B}(A \to ZH) \times \mathcal{B}(H \to ZZ) \times \mathcal{B}(ZZZ \to 4\ell)$. The observed (expected) upper limits are in the range of 0.031–0.539 (0.034–0.343) fb for the $R \to SH \to 4\ell + E_{\text{T}}^{\text{miss}}$ signal and 0.027–0.419 (0.035–0.335) fb for the $A \to ZH \to 4\ell + X$ signal ($X \equiv q\bar{q}/\ell^+\ell^-/\nu\bar{\nu}$).

Document created on 4th September 2023 using ATLAS LaTeX Version 14.5.0.

Analysis Team

[*email:* atlas-HDBS-2019-08-editors@cern.ch]

Bruce Mellado Garcia, Yaquan Fang, Theodota Lagouri, R D Schaffer, Ruanxf Ruan, Xin Shi, Abdualazem Fadol Mohammed, Humphry Tlou, Onesimo Mtintsilana

Editorial Board

Journal: JHEP

ATLAS Paper

HDBS-2019-08

4th September 2023

Draft version 0.5

Search for heavy resonances in final states with four leptons and missing transverse momentum or jets in pp collisions at $\sqrt{s} = 13$ TeV with the ATLAS detector

The ATLAS Collaboration

A search for a new heavy boson produced via gluon-fusion in the four-lepton channel with missing transverse momentum or jets is performed. The search uses proton–proton collision data equivalent to an integrated luminosity of 139 fb^{-1} at a centre-of-mass energy of 13 TeV collected by the ATLAS detector between 2015 and 2018 at the Large Hadron Collider. This study explores the decays of heavy bosons: $R \to SH$ and $A \to ZH$. In these processes, $S \to$ invisible and $H \to ZZ$. The Z boson associated with the heavy Higgs H decays into two leptons, jets, or invisible particles. The mass range of the heavy boson studied is 390–1300 (320–1300) GeV for the R (A) boson and 220–1000 GeV for the H boson. The mass of the S boson is set to a fixed value of 160 GeV. No significant deviation from the Standard Model backgrounds is observed. The results are interpreted as upper limits at a 95% confidence level on the $\sigma(gg \to R) \times \mathcal{B}(R \to SH) \times \mathcal{B}(H \to ZZ) \times \mathcal{B}(ZZ \to 4\ell)$ and $\sigma(gg \to A) \times \mathcal{B}(A \to ZH) \times \mathcal{B}(H \to ZZ) \times \mathcal{B}(ZZZ \to 4\ell)$. The observed (expected) upper limits are in the range of 0.031–0.539 (0.034–0.343) fb for the $R \to SH \to 4\ell + E_{\mathrm{T}}^{\mathrm{miss}}$ signal and 0.027–0.419 (0.035–0.335) fb for the $A \to ZH \to 4\ell + X$ signal ($X \equiv q\bar{q}/\ell^+\ell^-/\nu\bar{\nu}$).

Contents

1 Introduction **2**

2 The ATLAS detector **4**

3 Data and simulated event samples **4**

4 Object and event selection **6**
- 4.1 Object reconstruction 6
- 4.2 Event selection 7

5 Analysis strategy **8**

6 Signal and background modelling **10**
- 6.1 Signal model 10
- 6.2 Background model 10

7 Systematic uncertainties **12**
- 7.1 Experimental uncertainties 12
- 7.2 Theoretical uncertainties 13
- 7.3 Systematic uncertainties on backgrounds shapes 14

8 Statistical procedures **14**

9 Results **15**

10 Conclusion **21**

Appendix **23**

A Local p_0 values **23**

1 Introduction

In 2012, the ATLAS and CMS experiments independently discovered a new particle [1, 2]. The new particle's properties are consistent with the Higgs boson proposed by the Standard Model (SM) [3–6]. However, the SM still has several open questions, including dark matter, neutrino masses and mixing, the hierarchy problem, and the strong CP problem [7–9]. It is still debated whether the Higgs boson is a standalone particle or part of the Higgs sector suggested by the two-Higgs-doublet model (2HDM) [10, 11]. The 2HDM predicts the existence of five Higgs bosons, including a CP-even particle like the SM Higgs boson (h), a heavier Higgs boson (H), a CP-odd particle (A), and a charged Higgs scalar ($H^{\pm}$). Another extension of the SM is the 2HDM+S model [12, 13], which introduces a scalar boson (S) in addition to the 2HDM particles. The S boson is assumed to be a dark matter portal and a potential source of missing transverse momentum, achieved through its interaction with a pair of dark matter candidates ($\chi\chi$) [12].

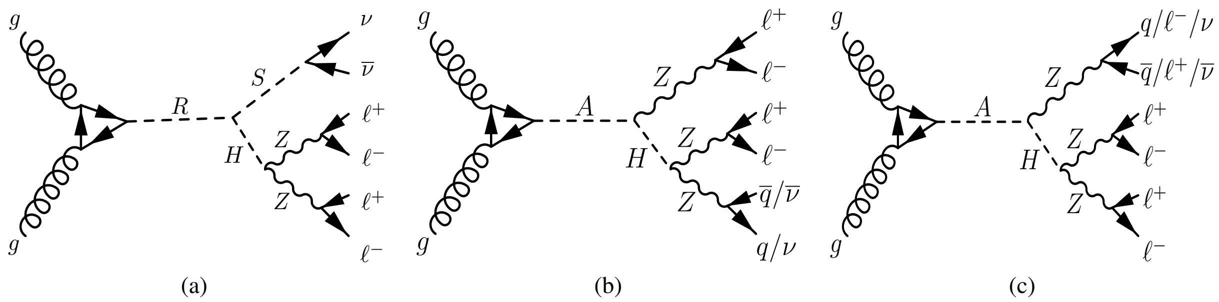

Figure 1: Feynman diagrams represent the production of heavy bosons via gluon-fusion at leading-order for the (a) $R \to SH \to 4\ell{+}E_{\mathrm{T}}^{\mathrm{miss}}$ signal, (b) $A \to Z(\to 2\ell)H(\to 2\ell{+}q\overline{q}/\nu\overline{\nu})$ signal, and (c) $A \to Z(\to q\overline{q}/\ell^{+}\ell^{+}/\nu\overline{\nu})H(\to 4\ell)$ signal, where ℓ could either be an electron or a muon, q represents a jet and ν denotes an invisible particle.

This paper aims to search for heavy resonances that decay to four leptons (4ℓ) and missing transverse momentum ($E_{\mathrm{T}}^{\mathrm{miss}}$) or jets ($q$), focusing on the high-mass region of the heavy bosons where the four-lepton invariant mass is above 200 GeV. This study uses proton–proton collision data at a centre-of-mass energy of 13 TeV and integrated luminosity of 139 fb^{-1} collected by the ATLAS detector in the 2015–2018 data taking period at the Large Hadron Collider (LHC). Two different scenarios are considered for the signal model. First, the 2HDM+S model includes only a heavy resonance H and Higgs-like scalar boson S. The model is extended to cover more general situations for various missing energy magnitudes by adding one heavy scalar R, where R decays to H and S bosons with $m_R > m_H + m_S$. The S boson decays into dark matter particles ($S \to$ invisible), and the H decays to 4ℓ through the decay of two Z bosons ($H \to ZZ \to 4\ell$). The masses of the R and H bosons are varied to control the missing transverse momentum, and the S mass is fixed to 160 GeV. The assumption of the S mass is motivated by the phenomenology study presented in Ref. [14]. However, we studied the effect of this choice and found that the S mass only affects the distribution of the missing transverse momentum if its mass is above 200 GeV. Therefore, fixing the S mass reduces the free parameters on the fit and simplifies the analysis. The phenomenology of the new $R \to SH$ topology can easily embed into the 2HDM+S model using an approach similar to that of Ref. [12]. Second, a 2HDM-based baryogenesis scenario is considered, which generates matter and antimatter asymmetry. This model is motivated by the equal amount of matter and antimatter supposedly generated in the early universe [15]. Searches for baryogenesis were conducted at the LHC with several channels, such as $H \to hh$ [16, 17], $H \to WW/ZZ$ [18–23] and $A \to Zh$ [24, 25]. Searches in the $A \to ZH \to 2\ell 2b/2\ell 2\tau$ [26–29] channels were also carried out at the LHC. In the latter case, for a strong first-order phase transition to occur in the early universe, the $m_A > m_H$ is preferred. Therefore, the $A \to ZH \to 4\ell + X$ model is added to this study to explore regions with jet activities where X could be two leptons, two jets or a pair of SM neutrinos. In this signal, A is a CP-odd scalar which decays to a CP-even scalar H and Z boson. Two decay possibilities are considered for the associated Z and H bosons: $A \to Z(\to \ell^{+}\ell^{-}/q\overline{q}/\nu\overline{\nu})H(\to 4\ell)$ and $A \to Z(\to 2\ell)H(\to 2\ell + q\overline{q}/\nu\overline{\nu})$, which are combined into one signal called the $A \to ZH \to 4\ell + X$ signal. In this analysis, only the gluon–gluon fusion production mode is considered for both the $R \to SH \to 4\ell + E_{\mathrm{T}}^{\mathrm{miss}}$ and $A \to ZH \to 4\ell + X$ signals, as illustrated by Feynman diagrams in Figure. 1.

This paper is organised as follows. The ATLAS experiment is described in Section 2. Section 3 describes the data and Monte Carlo samples, followed by the object reconstruction in Section 4. Section 5 describes the analysis strategy, and the signal and background modelling are discussed in Section 6. Section 7 demonstrates the experimental and theoretical systematic uncertainties. Section 8 explains the statistical model used in the analysis and the results are discussed in Section 9. The conclusion is given in Section 10.

2 The ATLAS detector

The ATLAS detector is a multipurpose particle physics detector at the LHC with cylindrical geometry[1] and forward-backwards symmetry [30]. It contains an inner tracking detector (ID) covered by a superconducting solenoid providing a 2 T magnetic field, electromagnetic (EM) and hadronic calorimeters, and a muon spectrometer with superconducting magnets. The ID has a silicon pixel, a silicon microstrip tracker, a transition radiation tracker, and an insertable silicon B-layer [31] covering the region $|\eta| < 2.5$. The calorimeter design includes lead/liquid-argon, steel/scintillator-tile, copper/liquid-argon, or tungsten/liquid-argon as the absorber fabric. It provides a pseudorapidity coverage of $|\eta| < 4.9$. The muon spectrometer (MS) incorporates superconducting toroidal air-core magnets around the calorimeters, which supply muon identification and momentum measurement for $|\eta| < 2.7$. A trigger system is employed at two stages to select events with an average rate of about 1 kHz for offline analysis [32].

3 Data and simulated event samples

The data used in this analysis were produced through proton–proton (pp) collisions at a centre-of-mass energy of 13 GeV recorded by the ATLAS detector at the LHC from 2015 to 2018. Events are required to satisfy data quality requirements to ensure the quality of the collected data [33–35]. After applying the event cleaning criteria, the total integrated luminosity of the entire data set reached 139 fb^{-1}.

Signal and background events were generated according to ATLAS detector configurations and utilised for signal optimisation, background parametrisation, and systematic uncertainty estimation. Each Monte Carlo (MC) event generator produced events that underwent ATLAS detector simulation [36] within the Geant4 framework [37]. The effect of multiple interactions in the same and neighbouring bunch crossings (pile-up) was modelled by overlaying the simulated hard-scattering event with inelastic pp events generated with Pythia 8.186 [38] at leading-order (LO) using the NNPDF2.3 LO set of parton distribution functions (PDF) [39] and the A3 set of tuned parameters [40].

The $q\bar{q} \to ZZ$ background process was simulated with the Sherpa 2.2.2 [41] using matrix elements at next-to-leading-order (NLO) accuracy in QCD for up to one additional parton and at LO accuracy for up to three additional parton emissions. The virtual QCD corrections were provided by the OpenLoops library [47–49]. The $gg \to ZZ$ background process was generated by Sherpa 2.2.2, including off-shell effects and Higgs boson contributions, using LO-accurate matrix elements for up to one additional parton emission. The $q\bar{q} \to ZZ$ (EW) events, consisting four leptons and two jets, were simulated using Sherpa 2.2.2. In addition, the VVV background events, including processes such as ZZZ, ZZW, and WWZ with at least

[1] ATLAS uses a right-handed coordinate system with its origin at the nominal interaction point (IP) in the centre of the detector and the z-axis along the beam pipe. The x-axis points from the IP to the centre of the LHC ring, and the y-axis points upwards. Cylindrical coordinates (r, ϕ) are used in the transverse plane, ϕ being the azimuthal angle around the z-axis. The rapidity is defined as $y = (1/2)\ln[(E + p_z)/(E - p_z)]$, where E is the energy and p_z is the longitudinal component of the momentum along the beam pipe. The polar angle θ as $\eta = -\ln\tan(\theta/2)$ defines the pseudorapidity. Angular distance is measured in units of $\Delta R \equiv \sqrt{(\Delta\eta)^2 + (\Delta\phi)^2}$.

Process	Generator and Parton shower	QCD accuracy	Tune and PDF
$R \to SH \to 4\ell + E_{\mathrm{T}}^{\mathrm{miss}}$	Pythia 8.244 [52]	LO	A14 and NNPDF2.3 LO [56, 64]
$A \to Z(\to q\bar{q}/\ell^+\ell^-/\nu\bar{\nu})H(\to 4\ell)$	MadGraph5_aMC@NLO 2.7.2 + Pythia 8.244 [51, 52]	LO	A14 and NNPDF2.3 LO [56, 64]
$A \to Z(\to 2\ell)H(\to 2\ell + q\bar{q}/\nu\bar{\nu})$	MadGraph5_aMC@NLO 2.7.2 + Pythia 8.244 [51, 52]	LO	A14 and NNPDF2.3 LO [56, 64]
$t\bar{t}V$ ($V = W/Z$)	MadGraph5_aMC@NLO 2.3.3 + Pythia 8.210 [51, 52]	LO	A14 and NNPDF2.3 LO [56, 64]
$q\bar{q} \to ZZ$	Sherpa 2.2.2 + MEPS@NLO [44–46]	NLO (0- and 1-jet), LO (2- and 3-jet)	Sherpa and NNPDF3.0 NNLO [50]
$gg \to ZZ$	Sherpa 2.2.2 + MEPS@NLO [44–46]	LO (0- and 1-jet)	Sherpa and NNPDF3.0 NNLO [50]
$q\bar{q} \to ZZ$ (EW)	Sherpa 2.2.2 + MEPS@NLO [44–46]	LO	Sherpa and NNPDF3.0 NNLO [50]
$ZZZ(4\ell 2\nu, 6\ell 0\nu)$	Sherpa 2.2.2 + MEPS@NLO [44–46]	NLO	Sherpa and NNPDF3.0 NNLO [50]
$WZZ(5\ell 1\nu)$	Sherpa 2.2.2 + MEPS@NLO [44–46]	NLO	Sherpa and NNPDF3.0 NNLO [50]
$WWZ(4\ell 2\nu)$	Sherpa 2.2.2 + MEPS@NLO [44–46]	NLO	Sherpa and NNPDF3.0 NNLO [50]
Z+jets	Sherpa 2.2.1 + MEPS@NLO [44–46]	NLO (0- and 2-jet), LO (3- and 4-jet)	Sherpa 2.2.1 and NNPDF3.0 NNLO [50]
$t\bar{t}$	Powheg-Box v2 + Pythia 8.230 [52–55]	NLO+LO	A14 and (NNPDF3.0 NLO & NNPDF2.3 LO) [56, 57, 64]
$WZ \to 3\ell 1\nu$	Powheg-Box v2 + Pythia 8.230 [52–55]	NLO	AZNLO and (CT10NLO & CTEQ6L1) [59–61]

Table 1: Summary of the event generators used for the simulated signal and background samples, including the accuracy of the matrix element and parton distribution functions (PDFs). Additionally, the table lists the set of tuned parameters used.

four prompt charged leptons, were simulated using Sherpa v2.2.2 with the NNPDF3.0 NNLO PDF set. The matrix element calculations for these processes were matched and merged with the Sherpa parton shower based on Catani–Seymour dipole factorisation [42, 43] using the MEPS@NLO prescription [44–46]. The NNPDF3.0 NNLO set of PDFs was used [50], along with the dedicated set of tuned parton-shower parameters developed by the Sherpa authors.

Events containing four prompt charged leptons coming from $t\bar{t}V$ background process ($V = Z$ or $W^\pm$) were modelled by MadGraph5_aMC@NLO 2.3.3 [51] and interfaced with Pythia 8.210 [52] for the hadronisation . The $t\bar{t}$ background was generated using Powheg-Box v2 [53–55] at NLO with the NNPDF30 NLO PDF set. The events were interfaced to Pythia 8.230 to model the parton shower, hadronisation, and underlying event, with parameters set according to the A14 tune [56] and using the NNPDF2.3 LO set of PDFs [39]. The decays of bottom and charm hadrons were performed by EvtGen 1.6.0 [57]. The Powheg-Box v2 generator was used to simulate the WZ [58] production process at NLO accuracy in QCD. Events were interfaced to Pythia 8.230 for the modelling of the parton shower, hadronisation, and underlying event, with parameters set according to the AZNLO tune [59]. The CT10 PDF set [60] was used for the hard-scattering processes, whereas the CTEQ6L1 PDF set [61] was used for the parton shower. The EvtGen 1.2.0 program was used to decay bottom and charm hadrons. The production of Z+jets was simulated with the Sherpa 2.2.1 generator using NLO matrix elements for up to two partons, and LO matrix elements for up to four partons calculated with the Comix [42] and OpenLoops libraries. They were matched with the Sherpa parton shower using the MEPS@NLO prescription using the set of tuned parameters developed by the Sherpa authors. The NNPDF3.0 NNLO set of PDFs was used and the samples were normalised to a next-to-next-to-leading-order (NNLO) prediction [62].

The $R \to SH \to 4\ell + E_{\mathrm{T}}^{\mathrm{miss}}$ signal was simulated using Pythia 8.244 with the A14 tune and NNPDF2.3 LO PDF set. The $A \to Z(\to q\bar{q}/\ell^+\ell^-/\nu\bar{\nu})H(\to 4\ell)$ and $A \to Z(\to 2\ell)H(\to 2\ell + q\bar{q}/\nu\bar{\nu})$ signals were generated by MadGraph5_aMC@NLO 2.7.2 with the A14 tune and NNPDF2.3 LO PDF set. The R mass considered in the range of 390–1300 GeV, with the S mass fixed to 160 GeV, and the A mass is in the range of 320–1300 GeV. The H mass value for all signal processes is in the range of 220–1000 GeV. Signals were generated using the narrow-width approximation (NWA) [63] in R and H widths for the $R \to SH \to 4\ell + E_{\mathrm{T}}^{\mathrm{miss}}$ signal and in A and H widths for the $A \to ZH \to 4\ell + X$ signal. In the NWA, the R, A, and H bosons are assumed to have negligible natural widths. Several signal mass points were generated using the Large-width approximation (LWA) to evaluate the impact of non-negligible natural widths. Table 1 summarise the generators, shower model, matrix element accuracy, tune, and PDF sets used in signal and background simulation.

4 Object and event selection

4.1 Object reconstruction

The event selection relies on reconstructing and identifying electrons, muons, jets and missing transverse momentum. The electron energy measurement is improved using a dynamic, topological calorimeter-cell clustering-based method. This method is particularly effective in cases where an electron radiates a bremsstrahlung photon. More information about this technique can be found in Ref. [65]. Electron candidates are identified as clusters of energy deposits in the calorimeter associated with ID tracks. The final track-cluster matching uses a Gaussian-sum filter (GSF) [66], accounting for bremsstrahlung energy losses. The electron's transverse momentum (p_{T}) is calculated from the cluster energy and the track direction at the interaction point. The rejection of background noise depends on the longitudinal and transverse shapes of the electromagnetic showers in the calorimeters, track-cluster matching, and properties of tracks in the ID. All this information, except for that related to track hits, is used to create a likelihood discriminant. The selection criteria combine the likelihood with the number of track hits and define several working points (WP). Electrons with $p_{\mathrm{T}} > 4.5$ GeV and pseudorapidity range $|\eta| < 2.47$ are selected. A "loose" WP with a 90% efficiency for electrons with $p_{\mathrm{T}} > 30$ GeV is also employed [67].

Muon reconstruction involves matching the track in the MS to the ID [68]. If a complete track is present in both detectors, a global fit is used to perform the matching. If hit information is only available from one of the detectors, the momentum is determined from the detector with hit information, and the track segment from the other detector is used for identification. This method, known as segment-tagged muon method, is used only in the central region of the barrel ($|\eta| < 0.1$), where the MS geometrical coverage is reduced. For an ID track with $p_{\mathrm{T}} > 15$ GeV, energy deposition in the calorimeter consistent with a minimum-ionizing particle is used to identify it as a muon (calorimeter-tagged muon). However, there is limited or no ID coverage in the forward region ($2.5 < |\eta| < 2.7$), and the MS track can be used for standalone muon identification or in combination with silicon hits if present in the forward ID (combined muon). To achieve good track reconstruction, ID tracks associated with muons must have a minimum number of associated hits in each ID sub-detector. Muons must have a minimum p_{T} of 5 GeV and a maximum $|\eta|$ of 2.7. Standalone muon candidates which traverse the MS must have hits in all three MS systems. This analysis uses a "loose" muon identification WP that uses all muon types and has an efficiency of 98.5% [68].

Fake leptons are suppressed using impact-parameter and track- and calorimeter-based isolation requirements. The transverse impact-parameter significance is the impact parameter calculated with respect to the measured beamline position in the transverse plane divided by its uncertainty, $|d_0|/\sigma_{d_0}$. This significance is required to be less than 3 for muons and less than 5 for electrons. Additionally, all leptons are required to be associated with the same originating vertex. These requirements help to ensure that leptons originate in hard interaction from a single object. Leptons must be isolated using both track-based and calorimeter-based discriminant. The track-based discriminants takes into account the scalar p_{T} sum of all tracks in the width cone $\Delta R = 0.3$ for muons and 0.2 for electrons (excluding the lepton itself). The ratio of this sum to the lepton p_{T} is expected to be less than 0.15. The pile-up contributions are suppressed by requiring the cone tracks to originate from the primary vertex. To retain efficiency at higher p_{T}, the size of the track-isolation cone is reduced to 10 GeV/p_{T} for p_{T} above 33 GeV for muons and above 50 GeV for electrons. Since the leptons must originate from a common vertex, the vertexing algorithm [82] is used to fit the ID tracks of the 4ℓ candidates under the assumption that they emanate from a common vertex. The resulting fit quality, represented by the χ^2/ndof value, provides good discrimination between signal and background.

For the 4μ channel, a cut of $\chi^2/\text{ndof} < 9$ is applied, while a loose cut of $\chi^2/\text{ndof} < 6$ is used for the other channels. This maintains a signal efficiency greater than 99% for all channels.

The reconstruction of jets applies a particle-flow algorithm [69], which combines measurements from the tracker and the calorimeter. The first step in jet reconstruction is to remove the energy deposited in the calorimeter by all charged particles. Then, the remaining calorimeter energy and tracks matched to the hard interaction are used to create particle-flow objects for the jet reconstruction. The charged-hadron measurement accuracy is enhanced while preserving the calorimeter measurements of neutral-particle energies, leading to an overall improvement. The anti-k_t algorithm uses a radius parameter $\Delta R = 0.4$ to reconstruct particle-flow jets [71]. After the jets are reconstructed, the jet four-momentum is recalibrated to the EM scale to remove the pile-up effect [72]. To further reduce the impact of pile-up jets, the jet-vertex-tagger (JVT) is used to select jets with $20 < p_{\mathrm{T}} < 60$ GeV and $|\eta| < 2.4$. The JVT uses a discriminant based on the projection of the missing transverse momentum from pile-up jets in the central region onto the forward jet [73, 74]. The used jets must be in the detector's central region within $|\eta| < 2.5$ with $p_{\mathrm{T}} > 30$ GeV.

Events containing b-hadrons (b-jets) are identified using a multivariate tagging algorithm (b-tagging) [75, 76]. This algorithm utilizes track impact parameters and reconstructed secondary vertices to determine the likelihood that a jet originates from b-quark hadronisation. It has an average efficiency of 77% for jets from b-quarks in simulated $t\bar{t}$-events with a rejection factor for light-flavour jets of around 30 [75].

After object reconstruction, an overlap-removal procedure is applied to all selected objects to remove ambiguities resulting from objects being reconstructed by several algorithms. The overlapping of objects is resolved by following the recommendations in Ref. [77]. As the same detector information can be used to reconstruct lepton and jet candidates, a procedure is applied to resolve the overlap ambiguities. The muon is selected when an electron and a muon share the same ID track. Unless the muon is calorimeter-tagged and is missing an MS track, the electron is selected. Reconstructed jets which overlap with electrons (muons) in a cone of size $\Delta R = \sqrt{(\Delta\eta)^2 + (\Delta\phi)^2} = 0.2\ (0.1)$ are removed.

The magnitude of the missing transverse momentum is denoted by $E_{\mathrm{T}}^{\mathrm{miss}}$ and is calculated as the negative sum of the transverse momenta of calibrated leptons and jets. Also, a soft term is included in the calculation, which is constructed from all tracks originating from the primary vertex[2] but not associated with any identified lepton or jet [78, 79].

4.2 Event selection

This analysis classifies events into three channels based on the flavours of the selected four leptons: 4μ, $4e$, and $2\mu 2e$. These channels are assigned based on the triggers activated in the event, which include single-lepton, dilepton, and trilepton triggers, with electron(s)-muon(s) triggers included in the latter two. The p_{T} thresholds of the triggers increase slightly during the data-taking period due to the rising luminosity [80, 81]. The p_{T} threshold increased from 20 to 26 GeV and 24 to 26 GeV for single-muon and single-electron triggers, respectively. Although the trigger thresholds varied between 2015 and 2017, their overall efficiency was roughly 98%.

The possible quadruplets in each channel of an event are created by up to two same flavour and opposite lepton pairs (SFOS). The p_{T} thresholds of the three leading leptons in the quadruplet follow this order: 20

[2] Selected events must have at least one vertex with two associated tracks with $p_{\mathrm{T}} > 500$ MeV, and the primary vertex is chosen to be the vertex with the largest $\sum p_{\mathrm{T}}^2$.

GeV, 15 GeV, and 10 GeV. The leading and the sub-leading lepton pairs in the quadruplet should have an invariant mass closest and second closest to the Z boson mass. The invariant mass of the leading and sub-leading lepton pairs are m_{Z_1} and m_{Z_2}, respectively. In the selected quadruplet, m_{Z_1} must be within 50 GeV $< m_{Z_1} <$ 106 GeV range, while m_{Z_2} must be within the 50 GeV $< m_{Z_2} <$ 115 GeV. The selected quadruplets must have their lepton pairs isolated from each other by $\Delta R > 0.1$. If any two SFOS leptons are detected with $m_{\ell\ell}$ below 5 GeV for 4μ and $4e$ quadruplets, the quadruplet is excluded to suppress the contamination from J/ψ mesons. In this analysis, the $Z + \Upsilon$ background contribution is negligible. If, at this point, several quadruplets of different channels are selected, only the quadruplet of the channel with the highest expected signal rate is retained, in the order: 4μ, $2e2\mu$, $4e$.

The resolution of the four lepton invariant mass system can be improved using a technique to recover the radiative photon production in the Z boson decay (final-state-radiation (FSR)) and a technique to apply constraints on the Z boson mass. In this analysis, the methodology presented in Ref. [83–85] for the $H \to ZZ$ analysis was used to account for FSR photons in the reconstruction of Z bosons, and for applying constraints on the Z boson mass. The Z-mass constraint is applied to both Z candidates and improves the resolution of $m_{4\ell}$ by around 15%. This analysis employs the combined 4μ, $4e$, and $2\mu2e$ channels, collectively called 4ℓ, to account for the limited statistics.

5 Analysis strategy

This analysis searches for heavy resonances that decay to four leptons and missing transverse momentum or jets where the four-lepton invariant mass is above 200 GeV. The main source of background in this kinematic region involves the leptonic decay of two Z bosons. Among the various background processes, quark-antiquark annihilation ($q\bar{q} \to ZZ$) is the most significant, contributing 84.6% of the expected background, while gluon-initiated production ($gg \to ZZ$) accounts for approximately 11.7%. Other SM backgrounds, such as $t\bar{t}V$, Z+jets, $t\bar{t}$, WZ, and VVV, account for about 2.6% of the total background events. These numbers are estimated from MC simulation after the four-lepton quadruplets selection discussed in Section 4.2. However, this study modelled the SM backgrounds using an analytical function, illustrated in Section 6, where the normalisation is taken from the data.

A cut-based optimisation was used to increase the sensitivity of the $R \to SH \to 4\ell + E_{\mathrm{T}}^{\mathrm{miss}}$ and $A \to ZH \to 4\ell + X$ signals. This involves setting thresholds on various kinematic and topological variables, such as the number of jets (n_{jets}) and b-jets ($n_{b\text{-jets}}$), the invariant mass of the two leading jets (m_{qq}), the momentum of the four-lepton system ($p_{\mathrm{T}}^{4\ell}$), and the $E_{\mathrm{T}}^{\mathrm{miss}}$ significance $\left(E_{\mathrm{T}}^{\mathrm{miss}}/\sqrt{\sum E_{\mathrm{T}}}\right)$. The aim is to separate signal events from background events and maximize the expected significance of the signals. To suppress top-related backgrounds such as $t\bar{t}$ and $t\bar{t}V$, events containing b-jets are vetoed. The remaining events are divided into two groups based on the number of jets: those with no jets ($n_{\mathrm{jets}} = 0$) and those with at least one jet ($n_{\mathrm{jets}} \geq 1$). A two-dimensional scan is applied twice to each group using the $p_{\mathrm{T}}^{4\ell}$ and $E_{\mathrm{T}}^{\mathrm{miss}}$ significance. The first scan determines the optimal threshold for the variables, and the second scan finds other optimal thresholds below the first ones. This process results in specific requirements on the variables that define the signal regions (SRs). The SR requirements depend on the number of jets and b-jets in the event. For events with no jets and no b-jets, $p_{\mathrm{T}}^{4\ell}$ must be greater than 20 GeV, and the $E_{\mathrm{T}}^{\mathrm{miss}}$ significance must be greater than 2. For events with at least one jet but no b-jets, $p_{\mathrm{T}}^{4\ell}$ must be greater than 10 GeV, and the $E_{\mathrm{T}}^{\mathrm{miss}}$ significance must be greater than 3.5. Events with at least one jet but no b-jets for the scan below the previous thresholds, the $E_{\mathrm{T}}^{\mathrm{miss}}$ significance is required to be greater than 2.5, and $p_{\mathrm{T}}^{4\ell} < 10$ GeV. Therefore, events in the SR are required to satisfy the following requirements:

- $n_{b\text{-jets}} = 0$ and $n_{\text{jets}} = 0$ with $p_{\text{T}}^{4\ell} > 20$ GeV and $E_{\text{T}}^{\text{miss}}$ significance > 2.0 (SR1)
- $n_{b\text{-jets}} = 0$ and $n_{\text{jets}} \geq 1$ with $p_{\text{T}}^{4\ell} > 10$ GeV and $E_{\text{T}}^{\text{miss}}$ significance > 3.5 (SR2)
- $n_{b\text{-jets}} = 0$ and $n_{\text{jets}} \geq 1$ with $p_{\text{T}}^{4\ell} < 10$ GeV and $3.5 > E_{\text{T}}^{\text{miss}}$ significance > 2.5 (SR3)

The SRs mentioned above are used for both the $R \to SH \to 4\ell + E_{\text{T}}^{\text{miss}}$ and the $A \to ZH \to 4\ell + X$ models. However, since the $A \to ZH \to 4\ell + X$ signal involves more jet activities, additional four-jet categories are defined as follows:

- Signal region four (SR4) requires events with no b-jets and at least two jets ($n_{\text{jets}} \geq 2$) within $|m_{qq} - m_Z| < 20$ GeV.
- Events with no b-jets and at least two jets which fall within $|m_{qq} - m_Z| > 20$ GeV are put into signal region six (SR5).
- Signal region seven (SR6) contains events with no b-jets and exactly one jet.
- Since we selected events with no b-jets in the previous categorisations, events with at least one b-jet ($n_{b\text{-jets}} \geq 1$) are required to account for the events containing b-jets (SR7).

Table 2 provides a summary of these seven SRs used in the analysis. Figure 2 shows a flowchart of SRs.

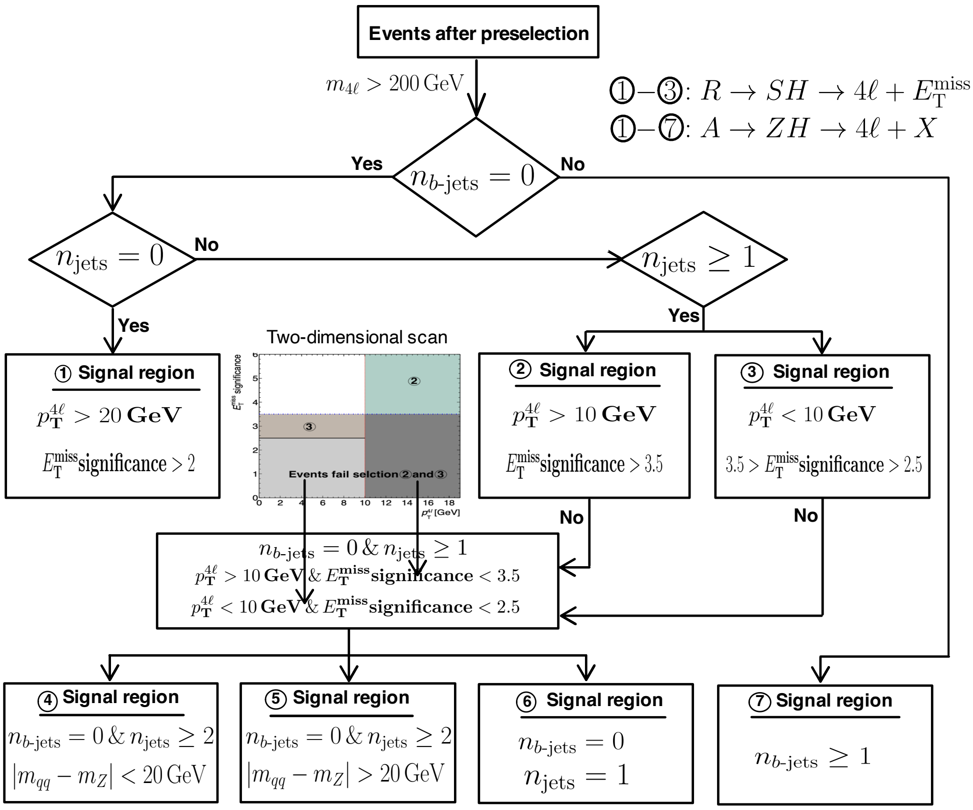

Figure 2: A flowchart diagram illustrating the signal regions for the $R \to SH \to 4\ell + E_{\text{T}}^{\text{miss}}$ and $A \to ZH \to 4\ell + X$ signals' optimisation. Three signal regions were developed for the $R \to SH \to 4\ell + E_{\text{T}}^{\text{miss}}$ signal, and seven signal regions for the $A \to ZH \to 4\ell + X$ signal. A two-dimensional scan was performed for the optimal selection of signal regions 2 and 3 (SR2 and SR3).

Signal region	$R \to SH \to 4\ell + E_{\mathrm{T}}^{\mathrm{miss}}$	$A \to ZH \to 4\ell + X$
SR1	$n_{b\text{-jets}} = 0$, $n_{\mathrm{jets}} = 0$, $p_{\mathrm{T}}^{4\ell} > 20$ GeV, $E_{\mathrm{T}}^{\mathrm{miss}}$ significance >2.0	$n_{b\text{-jets}} = 0$, $n_{\mathrm{jets}} = 0$, $p_{\mathrm{T}}^{4\ell} > 20$ GeV, $E_{\mathrm{T}}^{\mathrm{miss}}$ significance >2.0
SR2	$n_{b\text{-jets}} = 0$, $n_{\mathrm{jets}} \geq 1$, $p_{\mathrm{T}}^{4\ell} > 10$ GeV, $E_{\mathrm{T}}^{\mathrm{miss}}$ significance > 3.5	$n_{b\text{-jets}} = 0$, $n_{\mathrm{jets}} \geq 1$, $p_{\mathrm{T}}^{4\ell} > 10$ GeV, $E_{\mathrm{T}}^{\mathrm{miss}}$ significance > 3.5
SR3	$n_{b\text{-jets}} = 0$, $n_{\mathrm{jets}} \geq 1$, $p_{\mathrm{T}}^{4\ell} < 10$ GeV, 3.5 > $E_{\mathrm{T}}^{\mathrm{miss}}$ significance > 2.5	$n_{b\text{-jets}} = 0$, $n_{\mathrm{jets}} \geq 1$, $p_{\mathrm{T}}^{4\ell} < 10$ GeV, 3.5 > $E_{\mathrm{T}}^{\mathrm{miss}}$ significance > 2.5
SR4	–	$n_{b\text{-jets}} = 0$, $n_{\mathrm{jets}} \geq 2$, $\lvert m_{qq} - m_Z \rvert < 20$ GeV
SR5	–	$n_{b\text{-jets}} = 0$, $n_{\mathrm{jets}} \geq 2$, $\lvert m_{qq} - m_Z \rvert > 20$ GeV
SR6	–	$n_{b\text{-jets}} = 0$, $n_{\mathrm{jets}} = 1$
SR7	–	$n_{b\text{-jets}} \geq 1$

Table 2: The table summarising the requirements of the signal regions (SRs) selection for the $R \to SH \to 4\ell + E_{\mathrm{T}}^{\mathrm{miss}}$ and $A \to ZH \to 4\ell + X$ signals for $m_{4\ell} > 200$ GeV.

6 Signal and background modelling

MC simulation is used to parameterise the constructed four lepton invariant mass ($m_{4\ell}$) distribution for the SM backgrounds. Meanwhile, the signal shape is taken directly from the MC simulation, as illustrated below.

6.1 Signal model

A few mass points are generated for $R \to SH \to 4\ell + E_{\mathrm{T}}^{\mathrm{miss}}$ and $A \to ZH \to 4\ell + X$ signals, as demonstrated in Section 3. To cover a broader mass spectrum, a linear interpolation method described in Ref. [86] is used to get signal shapes between the generated masses in either of the (m_R, m_H) or (m_A, m_H) masses. Interpolating the signal involves a two-step process due to its dependence on either (m_R, m_H) or (m_A, m_H) masses. In the first step, the H mass remains constant while interpolating the $(m_R - m_H)$ or $(m_A - m_H)$ mass parameters or interpolating the R or A mass. Subsequently, the interpolated signals obtained in the previous step serve as input for a second interpolation. In this stage, the R or A mass is fixed, while the H mass varies by 10 GeV.

The interpolation was validated by comparing simulated and interpolated signal distributions at a few mass points, and a good agreement was found, as shown in Figure 3. Taking the difference as a systematic uncertainty had a negligible impact on the result and was hence omitted.

6.2 Background model

The $m_{4\ell}$ shape of the backgrounds is obtained from MC simulation using a parameterised empirical function to decrease statistical uncertainties originating from the limited number of simulated events. Four background templates are used: $q\bar{q} \to ZZ$, $gg \to ZZ$, VVV, and others. The VVV has a different shape from the rest of the backgrounds, so it is kept on a different template. Backgrounds such as $q\bar{q} \to ZZ$ (EW), $t\bar{t}V$, $t\bar{t}$, Z+jets and WZ. Each of the background templates is fitted with an analytical function for $m_{4\ell}$ between 200–1200 GeV, as follows:

$$f(m_{4\ell}) = H(m_0 - m_{4\ell}) f_1(m_{4\ell})\, C_1 + H(m_{4\ell} - m_0) f_2(m_{4\ell})\, C_2. \tag{1}$$

where:

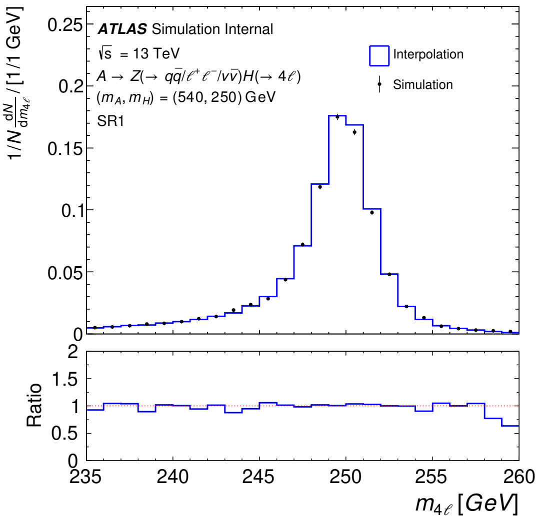

(a)

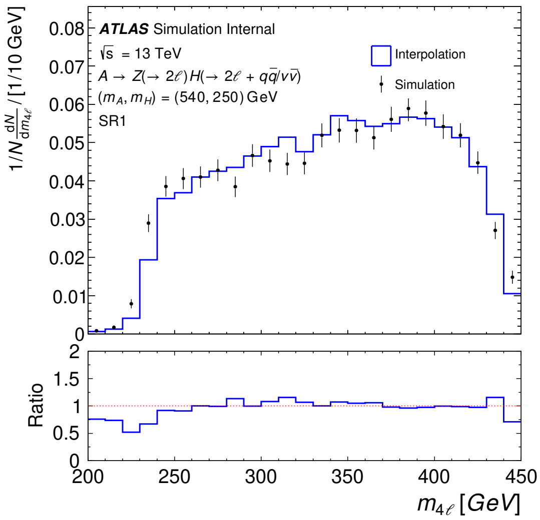

(b)

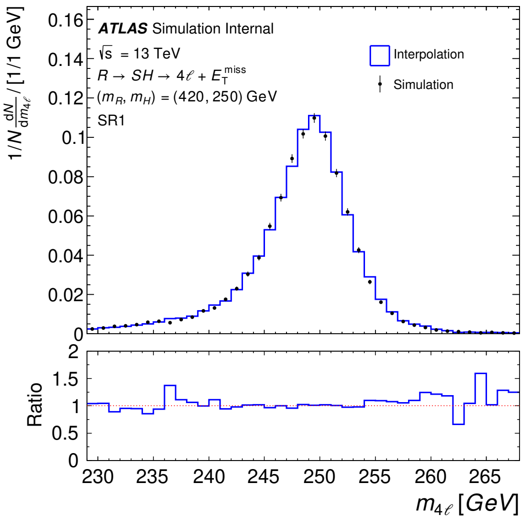

(c)

Figure 3: The $m_{4\ell}$ distributions of the interpolated (blue) and simulated (black-filled data point) signals for the (a) $A \to Z(\to q\overline{q}/\ell^+\ell^-/\nu\overline{\nu})H(\to 4\ell)$ and (b) $A \to Z(\to \ell^+\ell^-)H(\to 2\ell + q\overline{q}/\nu\overline{\nu})$ signals with the $(m_A, m_H) = (540, 250)$ GeV mass point and the (c) $R \to SH \to 4\ell + E_{\mathrm{T}}^{\mathrm{miss}}$ signal with $(m_R, m_H) = (420, 250)$ GeV and $m_S = 160$ GeV mass point. The lower panels show the ratio between the interpolated and simulated histograms.

$$f_1(m_{4\ell}) = \frac{a_1 \cdot m_{4\ell} + a_2 \cdot m_{4\ell}^2}{1 + \exp\left(\frac{m_{4\ell} - a_1}{a_3}\right)} \tag{2}$$

$$f_2(m_{4\ell}) = \left(1 - \frac{m_{4\ell}}{n_C}\right)^{b_1} \cdot \left(\frac{m_{4\ell}}{n_C}\right)^{\left(b_2 + b_3 \cdot \ln\left(\frac{m_{4\ell}}{n_C}\right)\right)} \tag{3}$$

$$C_1 = \frac{1}{f_1(m_0)}, \qquad C_2 = \frac{1}{f_2(m_0)}$$

The f_1 models the ZZ threshold around $2 \cdot m_Z$, and f_2 describes the high mass tail. The transition between the f_1 and f_2 functions is performed by the Heaviside step function $H(x)$ around m_0, where m_0 is fixed to 260, 240, 250 and 230 for the $q\bar{q} \to ZZ$, $gg \to ZZ$, VVV, and other backgrounds, respectively. The transition point is determined by optimising the function's smoothness. A constant $n_C = 13$ TeV scales the $m_{4\ell}$ in the high mass region. C_1 and C_2 ensure the continuity of the function around the m_0 corresponding to f_1 and f_2. Overall, a good fit quality was acquired with the empirical function in all signal regions (SRs). The integral error calculated from the fit function is considered a source of systematic uncertainty and is treated as a nuisance parameter during the final fit.

7 Systematic uncertainties

This section discusses the sources of systematic uncertainties considered in this analysis, including experimental and theoretical uncertainties for the signal and background processes. Statistical uncertainties arising from the MC event generation limitations are also considered. Additionally, uncertainties introduced by the background parameterisation are considered a source of uncertainty and propagated to the final fit. Each systematic component is treated as a nuisance parameter and profiled into the fit results. The systematic uncertainties are evaluated using the invariant mass of the four lepton system as a discriminant.

7.1 Experimental uncertainties

Experimental uncertainties, such as object reconstruction and identification, trigger efficiencies, energy scale, and resolution, are calculated for signal and background processes. The systematic experimental uncertainties are evaluated by computing the ratio between the integral of the $m_{4\ell}$ distribution with the interested nuisance parameter weight modified by one standard deviation and the integral of the $m_{4\ell}$ distribution using the nominal weight. The results are expressed as percentages for nuisance parameters with upward and downward variations corresponding to $\pm 1\sigma$. Signal samples were divided into three categories depending on the quantity of the energy gap ($m_A - m_H$ or $m_R - m_H$) to simplify estimating the experimental systematic uncertainties for the signals. The gaps include samples with low ($<$ 500 GeV), medium ($>$ 500 GeV and $<$ 700 GeV) and high ($>$ 1300 GeV) energy gaps. These ranges are for the $R \to SH \to 4\ell + E_{\mathrm{T}}^{\mathrm{miss}}$ process, and these ranges are slightly different for the $A \to ZH \to 4\ell + X$ process. The systematic uncertainties are evaluated for three signal mass points from each energy gap for both signals. Each result is combined by calculating the mean of the three samples per energy gap.

The uncertainty on the total integrated luminosity of the data recorded between 2015 and 2018 is ±1.7% [87]. In addition, systematic uncertainty introduced by re-scaling the simulated pile-up to the data is considered. The data scale factor is calculated using data to MC comparisons which comes with uncertainty. The current MC's nominal value is 1.0/1.03, scaled upward by 1.0/0.99 and downward by 1.0/1.07 to account for the pile-up re-weighting uncertainty [88]. It is estimated to be up to 2.5% for the $R \to SH \to 4\ell + E_{\mathrm{T}}^{\mathrm{miss}}$ signal, less than 1.0% for the $A \to ZH \to 4\ell + X$ signal, and about 3% for the VVV and other backgrounds.

The lepton identification, isolation and reconstruction efficiency, energy/momentum scale, and resolution are derived from data using $J/\psi \to \ell\ell$ and $Z \to \ell\ell$ decay events. The uncertainties in the lepton efficiency are calculated following the method presented in Refs. [67, 68] for muons and electrons. Generally, their effect on the signal yields is less than 1% for the $R \to SH \to 4\ell + E_{\mathrm{T}}^{\mathrm{miss}}$ signal, and up to 4% for the $A \to ZH \to 4\ell + X$ signal. These uncertainties are about 1.5% for the VVV background and roughly 1.7% for the other background. The uncertainties in the jet energy scale and resolution come from sources such as uncertainties in the absolute and relative "in situ" calibration and the correction for pile-up [72]. In total, uncertainties due to the jet energy scale and energy resolution are estimated to be 4.3% for the $R \to SH \to 4\ell + E_{\mathrm{T}}^{\mathrm{miss}}$ signal, 4.7% for the $A \to ZH \to 4\ell + X$ signal, approximately 7% for the VVV background and 10.4% for the other backgrounds. In addition, flavour tagging and jet-vertex-tagger (JVT) uncertainties due to disagreement in selecting the jet flavour are calculated by altering the uncertainty of the tagged jet flavour efficiency by $\pm 1\sigma$. The total estimated flavour tagging uncertainties are 4.3% for the $R \to SH \to 4\ell + E_{\mathrm{T}}^{\mathrm{miss}}$ and $A \to ZH \to 4\ell + X$ signals, 8.9% for the VVV background and 8.5% for the other backgrounds. The $E_{\mathrm{T}}^{\mathrm{miss}}$ is reconstructed using a signal associated with hard objects—namely muons, electrons, photons, hadronically decaying taus and jets. Objects not related to the hard ones are referred to as soft objects. The $E_{\mathrm{T}}^{\mathrm{miss}}$ uncertainty measurement is considered on the soft track term described in Ref. [89]. Two components were considered—the $E_{\mathrm{T}}^{\mathrm{miss}}$ parallel and perpendicular to hard objects momenta. The overall $E_{\mathrm{T}}^{\mathrm{miss}}$ uncertainty for the $R \to SH \to 4\ell + E_{\mathrm{T}}^{\mathrm{miss}}$ signal, and VVV background is less than 1%, about 6% for the $A \to ZH \to 4\ell + X$ signal, and 12.6% and 7.8% for the other backgrounds. The effect of these uncertainties on the shape is negligible therefore only the normalisation uncertainties are included.

7.2 Theoretical uncertainties

This analysis considers the effects of the parton distribution functions (PDFs), missing high-order QCD correction, initial- and final-state radiation (ISR/FSR), and parton showering (PS) and hadronisation uncertainties. The theoretical scale uncertainties on the signal samples are assessed by varying the factorisation and renormalisation scales up and down from their nominal values by a factor of two in each category. The scale uncertainty is the largest deviation in each category divided by the inclusive selections.

The PDF uncertainty is estimated using the SysCalc [90] package in conjunction with Madgraph. The uncertainty is determined by considering how the envelope of variations among alternative PDFs differs from the internal PDF error sets (NNPDF 3.0 PDF). The calculation follows the PDF4LHC recommendations provided in Ref. [91]. The ISR/FSR, PS and hadronisation uncertainties are evaluated by varying the signal eigen-variables in Pythia and comparing Herwig v7.1.3 [92] with Pythia for the signal samples. The overall theoretical uncertainty for the signal processes is about 1%. The theoretical systematic uncertainties on the SM background are included as a shape systematic and summarised below.

7.3 Systematic uncertainties on backgrounds shapes

To account for any possible biases introduced by the analytical function discussed in Section 6.2, uncertainties stemming from the background parameterisation are considered. These uncertainties are calculated by evaluating the error in the integral of the fitted function while also taking into account the errors in the parameters resulting from the fit. The errors are estimated using the correlation values obtained from the fit. The effect of uncertainty on the background shape is divided into two regions: 200 GeV $\leq m_{4\ell} \leq$ 700 GeV and 700 GeV $< m_{4\ell} \leq$ 1200 GeV.

Incorporating PDF and QCD scale uncertainties into the analysis is motivated by their impact on the shape of the $m_{4\ell}$ distributions for the $q\overline{q} \to ZZ$ and $gg \to ZZ$ processes. The QCD uncertainty is estimated to be up to 10% for the $q\overline{q} \to ZZ$ and $gg \to ZZ$ backgrounds. The PDF uncertainty is less than 25% for the $q\overline{q} \to ZZ$ and about 30% for the $gg \to ZZ$ background. A high-order electroweak correction (HOEW) uncertainty on the $m_{4\ell}$ shape is considered for the $q\overline{q} \to ZZ$ background, which is estimated to be less than 10%. A few nuisance parameters which affect the shape of the $m_{4\ell}$ distribution of the $q\overline{q} \to ZZ$ and $gg \to ZZ$ backgrounds are accounted for in this analysis. The parton-shower uncertainty is evaluated by varying parameters in the parton-shower tunes, such as the CKKW and QSF settings, and by using different showering options.

8 Statistical procedures

The invariant mass of the four leptons ($m_{4\ell}$) is utilised as a discriminant to examine the null and alternative hypotheses using the profile likelihood ratio technique [93]. The null hypothesis results in smoothed backgrounds that fall from the low mass range to the higher mass range of the $m_{4\ell}$ distribution. In contrast, the alternative hypothesis constructs a signal structure around the H mass. The signal and background contributions in the $m_{4\ell}$ distribution are extracted via a binned maximum-likelihood fit by the signal-plus background hypotheses to extract any indications for new physics. The profile likelihood function is defined by the probability of observing n events times the product sum of the weighted signal and background events, as shown below:

$$\mathcal{L}(m^{n}_{4\ell}|\sigma(gg \to A/R), \vec{\theta}) = \prod_{r=\mathrm{SRs}}^{n_r} \prod_{b=\mathrm{bin}}^{n_b} \mathrm{Poisson}\left(n_{r,b} \mid S_{r,b} + \sum_{B} B_{r,b}(\vec{\theta})\right) \times \prod_{i} G_i(0|\vec{\theta}, 1), \quad (4)$$

where $\sigma(gg \to A/R)$ is the parameter of interest for the $A \to ZH \to 4\ell + X$ or $R \to SH \to 4\ell + E_{\mathrm{T}}^{\mathrm{miss}}$ signal. The expected signal and background yields in each $m_{4\ell}$ distribution bin are represented by the S and B, respectively. The expected signal yields S is calculated by:

$$S = \sigma(gg \to A/R) \times \mathcal{B}(A/R \to ZH/SH) \times \mathcal{B}(H \to ZZ) \times \mathcal{B}(ZZZ/ZZ \to 4\ell) \times AC \times \int L \, \mathrm{d}t, \quad (5)$$

where AC is the acceptance times the efficiency, and $\int L \, \mathrm{d}t = 139 \text{ fb}^{-1}$ is the integrated luminosity of the data. A collection of nuisance parameters is introduced to describe how systematic uncertainties influence the predicted number of signal and background events and the shape of the PDFs. These parameters are constrained to their nominal values within the calculated uncertainties using Gaussian constraints by $G(\vec{\theta})$,

	SR1	SR2	SR3	SR4	SR5	SR6	SR7
$q\bar{q} \to ZZ$	132.2 ± 12	17.1 ± 6	41.9 ± 6.8	86.3 ± 11.4	39.8 ± 6.6	156.2 ± 12.7	549.6 ± 70.5
$gg \to ZZ$	31.9 ± 5.8	3.2 ± 3.1	8.3 ± 3.1	9.4 ± 4.2	6.6 ± 2.8	22.1 ± 3.6	101.5 ± 71.5
VVV	7.5 ± 0.4	4.8 ± 0.3	1.5 ± 0.2	00.5 ± 0.1	0.2 ± 0	1.1 ± 0.1	1.6 ± 0.1
other	5.5 ± 0.9	7.1 ± 1.1	3.6 ± 0.7	37.6 ± 2.3	2.5 ± 0.3	17.5 ± 0.8	11.2 ± 0.8
μ^{ZZ}_{norm}	1.2 ± 0.2	1.3 ± 0.6	1 ± 0.2	1.4 ± 0.3	0.9 ± 0.2	0.8 ± 0.1	1.2 ± 0.1
Total background	177.1 ± 13.3	32.1 ± 5.6	55.3 ± 7.4	133.8 ± 11.6	49 ± 7	196.9 ± 14	664 ± 26.1
Observed	177	32	55	135	49	197	664

Table 3: Observed and expected post-fit event yields for $m_{4\ell} > 200$ GeV with their uncertainties. The expected yields and their uncertainties are obtained from a simultaneous fit to data under the background-only hypothesis on all seven signal regions (SRs) discussed in Section 5. The μ^{ZZ}_{norm} is the normalisation factor for the $q\bar{q} \to ZZ$ and $gg \to ZZ$ backgrounds which is considered during the fit. The other background includes $q\bar{q} \to ZZ$ (EW), $t\bar{t}V$, $t\bar{t}$, Z+jets and WZ processes.

in which $\vec{\theta}$ is a vector containing the nuisance parameters. The dependence of the analysis on SRs for each event is indicated in the product by the index "r". In each SR, the normalisation for the $q\bar{q} \to ZZ$ and $gg \to ZZ$ processes (ZZ background) are calculated by a likelihood fit to the data. The ZZ background normalisation is denoted by the μ^{ZZ}_{norm} parameter. The benefit of taking the ZZ background normalisation from the data is the reduction in the background dependence on the theoretical systematic uncertainties.

9 Results

Table 3 displays the yields in each of the seven SRs described in Section 5. The observed and expected numbers of events in each SR were obtained using a simulated binned maximum-likelihood fit, assuming the background-only hypothesis. We performed signal-plus-background binned maximum-likelihood fits on the $m_{4\ell}$ distribution to search for potential excesses beyond the expected SM backgrounds. This fit model is based on the statistical framework discussed in Section 8. We scanned the m_R (m_A) range 390–1300 (320–1300) GeV and the m_H range 220–1000 GeV for the $R \to SH \to 4\ell + E_{\text{T}}^{\text{miss}}$ ($A \to ZH \to 4\ell + X$) signal. The fit was performed in steps of 10 GeV, in which 4187 (m_R, m_H) and 4740 (m_A, m_H) mass points in NWA for each SR were tested for the $R \to SH \to 4\ell + E_{\text{T}}^{\text{miss}}$ and $A \to ZH \to 4\ell + X$ processes, respectively. The resulting test statistics were used to construct p-values and significance estimates, which were then used to evaluate the compatibility of the data with the background-only hypothesis and the presence of new physics in the data.

The four lepton invariant mass distributions for the $R \to SH \to 4\ell + E_{\text{T}}^{\text{miss}}$ signal with the $(m_R, m_H) = (500, 300)$ GeV mass point in all three SRs are shown in Figure 4. Figures 5 and 6 show the $m_{4\ell}$ distribution in the seven SRs defined for the $A \to ZH \to 4\ell + X$ signal with the $(m_A, m_H) = (510, 380)$ GeV mass point. No significant deviation from the SM backgrounds is observed in the data. The p values as a function of the m_R/m_A and m_H are shown in Appendix A. Excesses, around 2.0 standard deviations, for a few mass points are shown in Figure 8(a) for the $R \to SH \to 4\ell + E_{\text{T}}^{\text{miss}}$ signal and in Figure 8(b) for the $A \to ZH \to 4\ell + X$ signal. The most significant excess comes from the $A \to ZH \to 4\ell + X$ signal at the $(m_A, m_H) = (510, 380)$ GeV mass point with a local significance of 2.5 standard deviations. The impact of

$R \to SH \to 4\ell + E_{\mathrm{T}}^{\mathrm{miss}}$			$A \to ZH \to 4\ell + X$		
(m_R, m_H) [GeV]	Uncertainty source	$\Delta\sigma/\sigma$ [%]	(m_A, m_H) [GeV]	Uncertainty source	$\Delta\sigma/\sigma$ [%]
	Jet flavour composition	6.2		others parameterisation SR4	5
	Jet flavour response	4.8		$q\bar{q} \to ZZ$ parameterisation SR4	3.9
$(390, 220)$	Pile-up reweighting	4.0	$(320, 220)$	Jet flavour composition	3.9
	Jet energy scale	4.2		Luminosity	3.7
	CKKW parton showering ($gg \to ZZ$) SR2	3.8		$gg \to ZZ$ parameterisation SR7	3.6
	CKKW parton showering ($gg \to ZZ$) SR2	3.1		Luminosity	2.4
	QSF parton showering ($gg \to ZZ$) SR2	3		Jet flavour composition	2.4
$(500, 300)$	$q\bar{q} \to ZZ$ parameterisation SR2	2	$(510, 380)$	Jet energy scale	1.7
	Pile-up reweighting	1.9		Jet energy resolution	1.5
	VVV parameterisation SR2	1.9		Signal PDF	1.4
	$q\bar{q} \to ZZ$ parameterisation SR2	9.3		CKKW parton showering ($gg \to ZZ$) SR2	3.3
	Jet flavour composition	7.3		QSF parton showering ($gg \to ZZ$) SR2	3.3
$(1300, 1000)$	Jet flavour response	3.5	$(1300, 1000)$	others parameterisation SR2	2.6
	Pile-up reweighting	2.9		$q\bar{q} \to ZZ$ parameterisation SR6	2.1
	CKKW parton showering ($gg \to ZZ$) SR2	2.9		VVV parameterisation SR2	2.1

Table 4: The impact of the most important sources of uncertainty on the parameter of interest (cross section) for three mass points for each $R \to SH \to 4\ell + E_{\mathrm{T}}^{\mathrm{miss}}$ and $A \to ZH \to 4\ell + X$ signals after the fit. The quadrature sum of the upward and downward effect ($\Delta\sigma$) is divided by the best fit value of the signal strength (σ) for each signal. The cross section of each signal times the branching ratio was set to the expected upper limit. Shape uncertainties are uncorrelated and hence affect each region separately.

systematic uncertainties on the analysis is investigated using the parameter of interest (cross section) for the $R \to SH \to 4\ell + E_{\mathrm{T}}^{\mathrm{miss}}$ and $A \to ZH \to 4\ell + X$ signals. The uncertainties that have the most significant impact vary depending on the choice of the (m_R, m_H) or (m_A, m_H) mass points. Table 4 shows the relative uncertainties in the σ, best-fit value, from the leading sources of systematic uncertainty for three different mass points for each signal. The effect of the uncertainties is estimated using Asimov data produced with the signal cross section set to the expected limits for the particular (m_R, m_H) or (m_A, m_H) mass points, assuming a narrow-width R or A and H bosons. As no significant excess was observed in comparison to the background predictions, the results were translated into upper limits on the production cross-section of the $R \to SH \to 4\ell + E_{\mathrm{T}}^{\mathrm{miss}}$ and $A \to ZH \to 4\ell + X$ signals times the branching fractions. The branching fractions considered are $\mathcal{B}(R \to SH)$, $\mathcal{B}(H \to ZZ)$ and $\mathcal{B}(ZZ \to 4\ell)$ for the $R \to SH \to 4\ell + E_{\mathrm{T}}^{\mathrm{miss}}$ process. For the $A \to ZH \to 4\ell + X$ process, the branching fractions are $\mathcal{B}(A \to ZH)$, $\mathcal{B}(H \to ZZ)$ and $\mathcal{B}(ZZZ \to 4\ell)$.

The CL$_s$ approach in the asymptotic approximation [93, 95] calculates the upper limit at 95% confidence level (CL) on the explored phase space. The upper limit, either on $\sigma(gg \to R) \times \mathcal{B}(R \to SH) \times \mathcal{B}(H \to ZZ) \times \mathcal{B}(ZZ \to 4\ell)$ or on $\sigma(gg \to A) \times \mathcal{B}(A \to ZH) \times \mathcal{B}(H \to ZZ) \times \mathcal{B}(ZZZ \to 4\ell)$, for a specific mass hypothesis, is obtained by fixing the H mass parameter to a constant value and optimising the probability function for nuisance parameters. The observed and expected upper limits of NWA R and H bosons for the $R \to SH \to 4\ell + E_{\mathrm{T}}^{\mathrm{miss}}$ signal are shown in Figures 7(a) and 7(b) in the (m_H, m_R) plane where the z-axis displays the $\sigma(gg \to R) \times \mathcal{B}(R \to SH) \times \mathcal{B}(H \to ZZ) \times \mathcal{B}(ZZ \to 4\ell)$ in the unit of fb. The upper limits for the $R \to SH \to 4\ell + E_{\mathrm{T}}^{\mathrm{miss}}$ signal range from 0.031 fb for the $(m_R, m_H) = (1300, 980)$ GeV to 0.539 fb for the $(m_R, m_H) = (410, 240)$ GeV. In contrast, the expected upper limits vary from 0.035 fb to 0.318 fb for the same mass points. Similarly, Figures 7(c) and 7(d) show the observed and expected upper limits for the $A \to ZH \to 4\ell + X$ signal in the (m_H, m_A) plane, in which the z-axis represents the upper limits on the $\sigma(gg \to A) \times \mathcal{B}(A \to ZH) \times \mathcal{B}(H \to ZZ) \times \mathcal{B}(ZZZ \to 4\ell)$. For the $A \to ZH \to 4\ell + X$ signal, the upper limits run from 0.027 fb for the $(m_A, m_H) = (1300, 760)$ GeV to 0.419 fb for the $(m_A, m_H) = (430, 240)$ GeV, whereas the corresponding expected upper limits range from

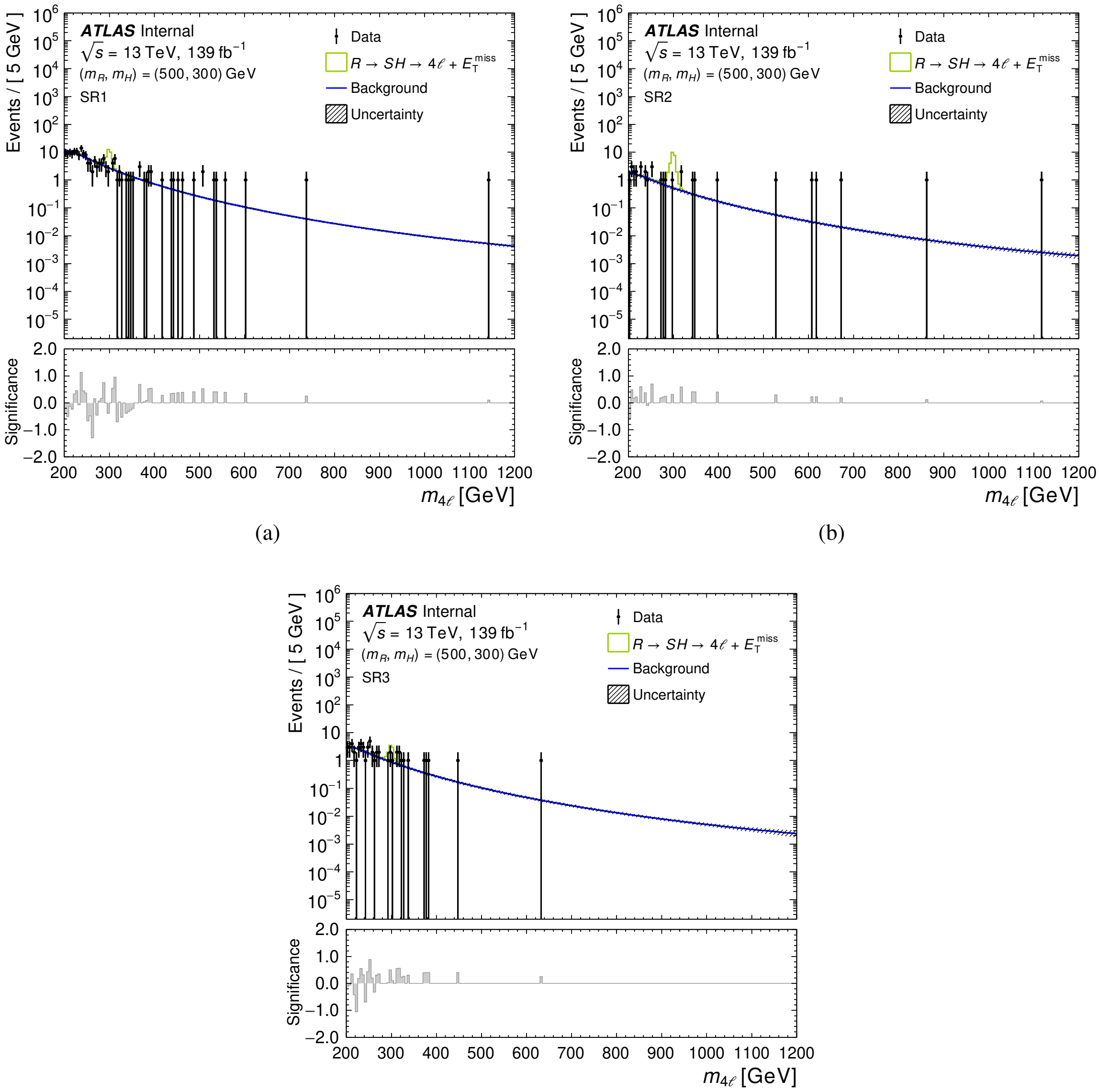

(a) (b) (c)

Figure 4: Observed and expected distributions of the invariant mass of the four-lepton system in the $R \to SH \to 4\ell + E_{\mathrm{T}}^{\mathrm{miss}}$ search for (a) SR1, (b) SR2 and (c) SR3 under a background-only fit to data. The total background (blue) includes the $q\overline{q} \to ZZ$, $gg \to ZZ$, $q\overline{q} \to ZZ$ (EW), VVV, $t\bar{t}V$, $t\bar{t}$, Z+jets and WZ processes. The distribution of the $(m_R, m_H) = (500, 300)$ GeV signal (green) is normalised to 50 times the observed upper limit (5.7 fb) discussed in Section 9. The hatched lines show the systematic uncertainty of the Monte Carlo (MC) prediction, while the error bar on the data denotes the statistical uncertainty. The lower panel displays the significance of each bin, which is determined by the residual of the data corresponding to the fitted background taking the statistical uncertainty of the data into account. The recommended significance formula in Ref. [94] is used in the calculation.

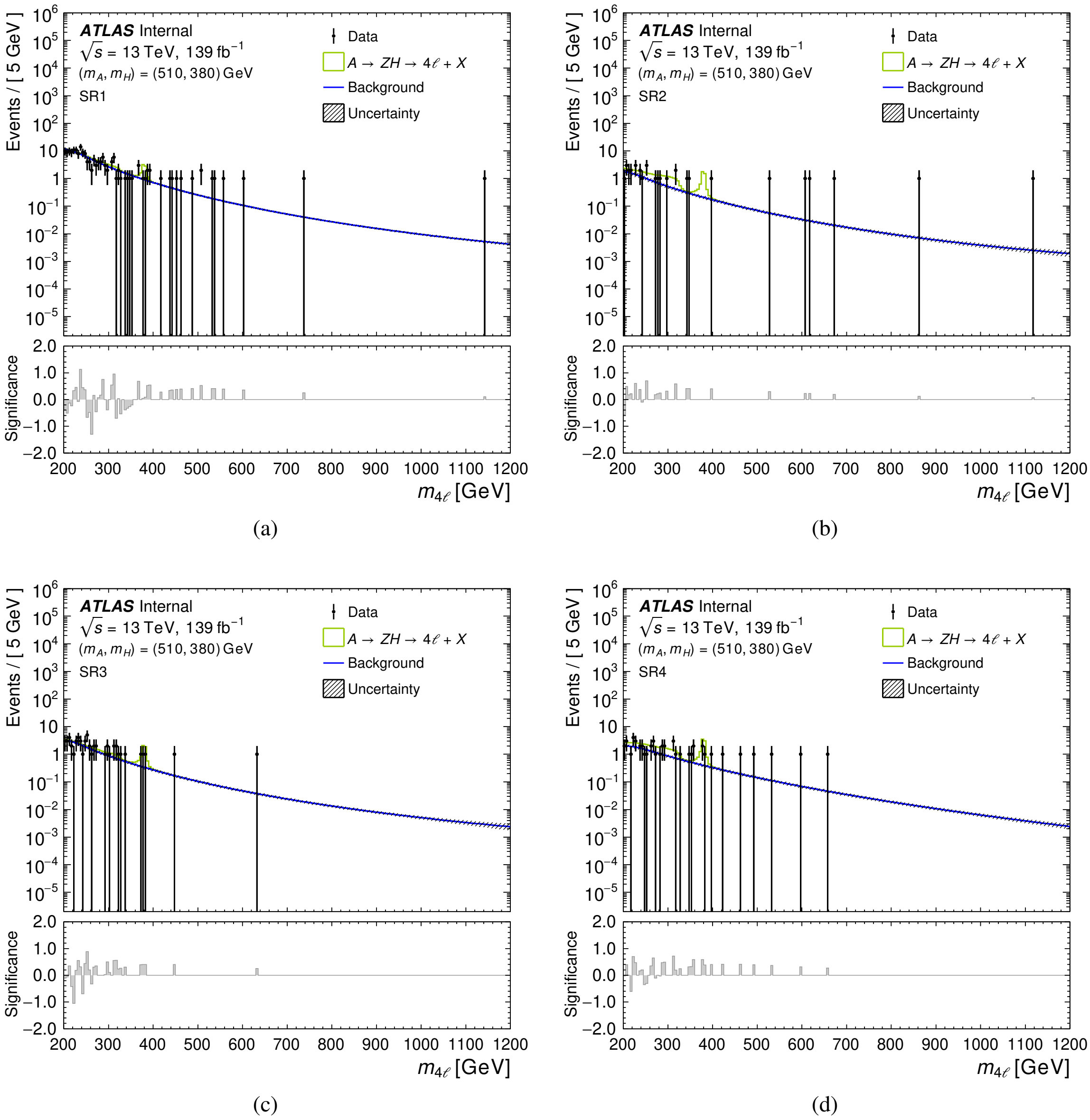

Figure 5: Observed and expected distributions of the invariant mass of the four-lepton system in the $A \rightarrow ZH \rightarrow 4\ell + X$ search for (a) SR1, (b) SR2, (c) SR3 and (d) SR4 under a background-only fit to data. The total background (blue) includes the $q\bar{q} \rightarrow ZZ$, $gg \rightarrow ZZ$, $q\bar{q} \rightarrow ZZ$ (EW), VVV, $t\bar{t}V$, $t\bar{t}$, Z+jets and WZ processes. The distribution of the $(m_A, m_H) = (510, 380)$ GeV signal (green) is normalised to 50 times the observed upper limit (18 fb) discussed in Section 9. The hatched lines show the systematic uncertainty of the Monte Carlo (MC) prediction, while the error bar on the data denotes the statistical uncertainty. The lower panel displays the significance of each bin, which is determined by the residual of the data corresponding to the fitted background taking the statistical uncertainty of the data into account. The recommended significance formula in Ref. [94] is used in the calculation.

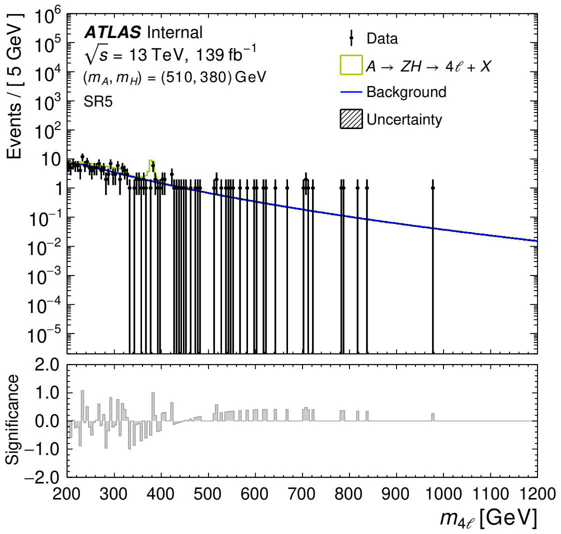

(a)

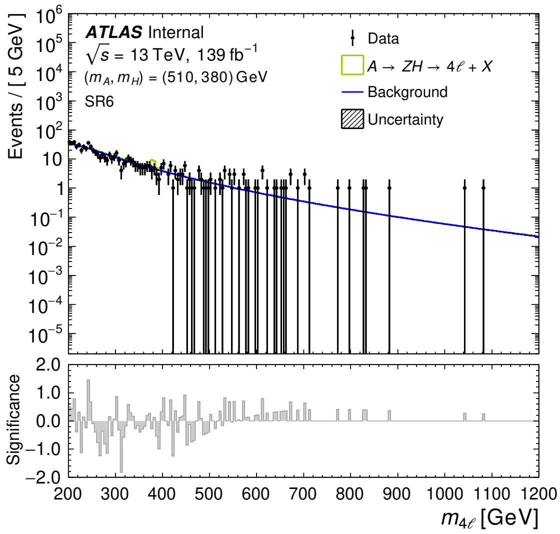

(b)

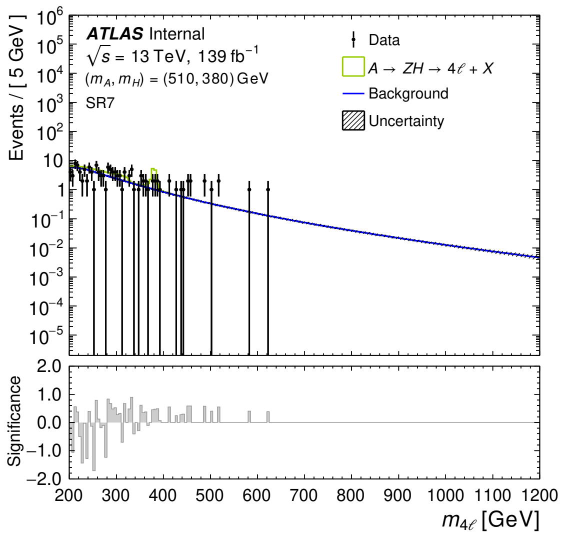

(c)

Figure 6: Observed and expected distributions of the invariant mass of the four-lepton system in the $A \to ZH \to 4\ell+X$ search for (a) SR5, (b) SR6 and (c) SR7 under a background-only fit to data. The total background (blue) includes the $q\bar{q} \to ZZ$, $gg \to ZZ$, $q\bar{q} \to ZZ$ (EW), VVV, $t\bar{t}V$, $t\bar{t}$, Z+jets and WZ processes. The distribution of the (m_A, m_H) = (510, 380) GeV signal (green) is normalised to 50 times the observed upper limit (18 fb) discussed in Section 9. The hatched lines show the systematic uncertainty of the Monte Carlo prediction, while the error bar on the data denotes the statistical uncertainty. The lower panel displays the significance of each bin, which is determined by the residual of the data corresponding to the fitted background taking the statistical uncertainty of the data into account. The recommended significance formula in Ref. [94] is used in the calculation.

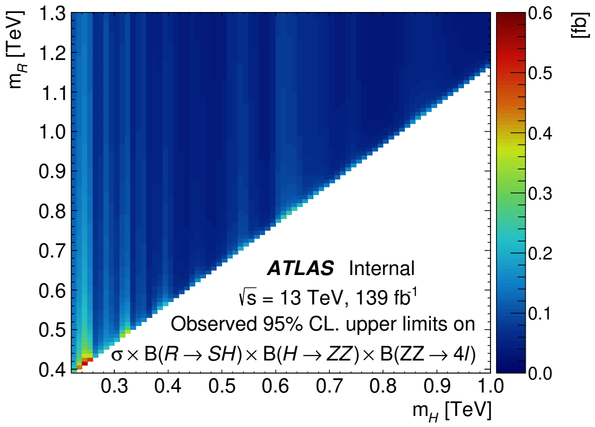

(a)

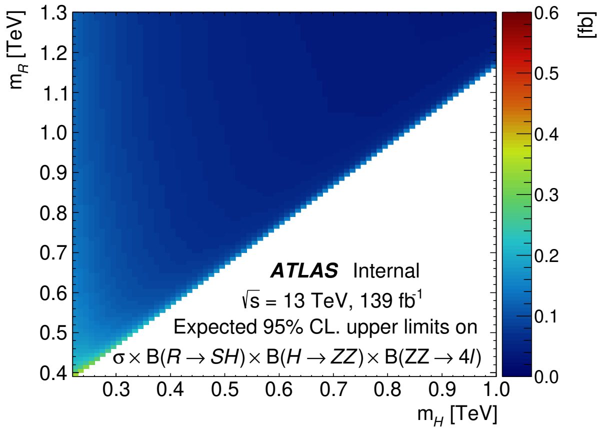

(b)

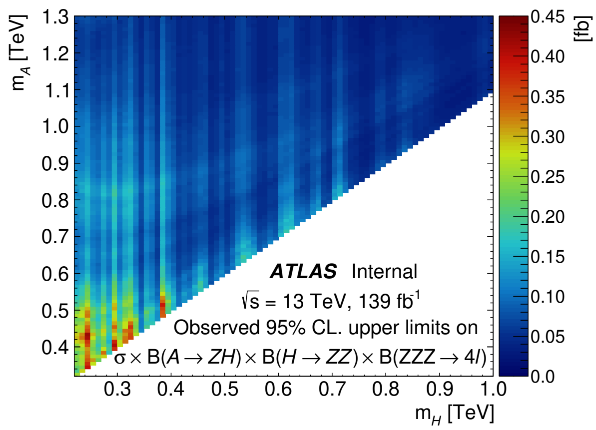

(c)

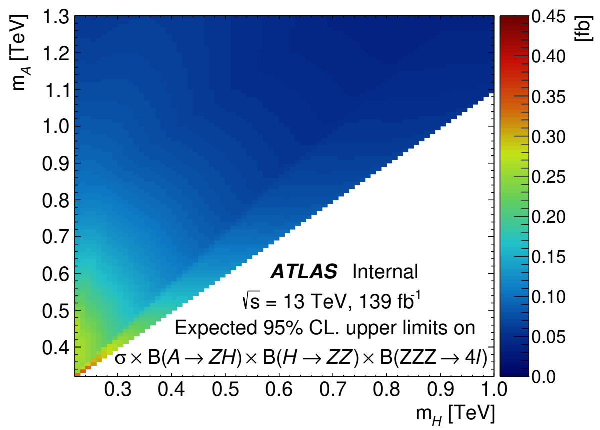

(d)

Figure 7: The observed (left) and expected (right) upper limits at 95% confidence level in (a), (b) the $\sigma(gg \to R) \times \mathcal{B}(R \to SH) \times \mathcal{B}(H \to ZZ) \times \mathcal{B}(ZZ \to 4\ell)$ on the (m_H, m_R) plane with $m_S = 160$ GeV for the $R \to SH \to 4\ell + E_{\mathrm{T}}^{\mathrm{miss}}$ signal, and in (c), (d) the $\sigma(gg \to A) \times \mathcal{B}(A \to ZH) \times \mathcal{B}(H \to ZZ) \times \mathcal{B}(ZZZ \to 4\ell)$ on the (m_H, m_A) plane for the $A \to ZH \to 4\ell + X$ signal.

0.038 fb to 0.244 fb. The upper limits are also calculated using pseudo-experiments to check the validity of the asymptotic approach at high H boson mass where the statistic is limited for a few mass points. The observed (expected) upper limits using the asymptotic approach are underestimated by 10% (1%) for the $R \to SH \to 4\ell + E_{\mathrm{T}}^{\mathrm{miss}}$ signal and by 15% (3%) for the $A \to ZH \to 4\ell + X$ signal.

The analysis focused on studying heavy resonances with NWA A or R and H bosons produced via gluon-gluon fusion for the $A \to ZH \to 4\ell + X$ and $R \to SH \to 4\ell + E_{\mathrm{T}}^{\mathrm{miss}}$ processes. However, it would be interesting to study the effect of the large-width approximation (LWA) in a similar scenario. Two low and high mass points, $(m_A, m_H) = (320, 220)$ GeV and $(m_A, m_H) = (1190, 600)$ GeV, for the $A \to ZH \to 4\ell + X$ signal were generated using similar configurations as for the NWA signal, to give an insight into this. Upper limits are computed for signal assumptions in which the A and H bosons have a significant natural width relative to the experimental mass resolution. The upper limit decreases as the natural width of the A and H bosons increases. For example, in the case of an $A \to ZH \to 4\ell + X$ signal

Width assumptions	Mass points [GeV]	Upper limits in the $\sigma(gg \to A)$ [fb]		Fractions
		Observed	Expected	
Narrow width	$(m_A, m_H) = (320, 220)$	0.254	0.325	–
	$(m_A, m_H) = (1190, 600)$	0.062	0.046	–
$(\Gamma_A/m_A, \Gamma_H/m_H) = (15\%, 5\%)$	$(m_A, m_H) = (320, 220)$	0.409	0.470	1.4
	$(m_A, m_H) = (1190, 600)$	0.109	0.077	1.7
$(\Gamma_A/m_A, \Gamma_H/m_H) = (30\%, 10\%)$	$(m_A, m_H) = (320, 220)$	0.504	0.551	1.7
	$(m_A, m_H) = (1190, 600)$	0.115	0.085	1.9

Table 5: Observed and expected upper limits at 95% confidence level (CL) on the $\sigma(gg \to A) \times \mathcal{B}(A \to ZH) \times \mathcal{B}(H \to ZZ) \times \mathcal{B}(ZZZ \to 4\ell)$ of different large-width approximation (LWA) signals for comparison with the narrow-width approximation (NWA) signal. The fraction is the ratio between the expected LWA's upper limit and the expected NWA's upper limit. The Γ_A and Γ_H denote the widths of the A and H bosons, respectively.

that produces A and H bosons with natural widths of 15% and 5%, respectively, of their experimental mass resolution, the upper limit declined by a factor of 1.4 for the low mass point and 1.7 for the high mass point compared to the NWA upper limit. In the $(\Gamma_A/m_A, \Gamma_H/m_H) = (30\%, 10\%)$ case, the upper limit is reduced by a factor of 1.7 for the low mass point and by a factor of 1.9 for the high mass point comparing to the NWA scenario. Table 5 summarises width assumptions, mass points and upper limits for the LWA and the NWA.

10 Conclusion

A search is performed for new heavy resonances in a final state with four leptons and missing transverse energy or jets. The search uses proton-proton collision data at a centre-of-mass energy of 13 TeV collected by the ATLAS detector from 2015 to 2018 at the Large Hadron Collider with a total integrated luminosity of 139 fb^{-1}. The search focused on two signal processes: $R \to SH \to 4\ell + E_{\mathrm{T}}^{\mathrm{miss}}$ and $A \to ZH \to 4\ell + X$. For the $R \to SH \to 4\ell + E_{\mathrm{T}}^{\mathrm{miss}}$ signal, the R boson decays to S and H bosons, where $S \to \nu\nu$ and $H \to ZZ \to 4\ell$. In the $A \to ZH \to 4\ell + X$ signal, the A boson decays to Z and H bosons, with two possible decay modes considered for the associated Z and H bosons: $A \to Z(\to q\bar{q}/\ell^+\ell^-/\nu\bar{\nu})H(\to 4\ell)$ and $A \to Z(\to 2\ell)H(\to 2\ell + q\bar{q}/\nu\bar{\nu})$. For both the $A \to ZH \to 4\ell + X$ and $R \to SH \to 4\ell + E_{\mathrm{T}}^{\mathrm{miss}}$ processes, the heavy boson H mass is between 220 GeV and 1000 GeV. The mass range considered for the hypothetical resonance is in the range of 320–1300 GeV for the A boson and 390–1300 GeV for the R boson, while the S boson mass is fixed at 160 GeV.

No significant deviation above the SM backgrounds is observed. The highest excess observed in the data is at the $(m_A, m_H) = (510, 380)$ GeV mass point with 2.5σ for the $A \to ZH \to 4\ell + X$ signal. A few excesses at several (m_R, m_H) and (m_A, m_H) mass hypotheses are reported for the $R \to SH \to 4\ell + E_{\mathrm{T}}^{\mathrm{miss}}$ and $A \to ZH \to 4\ell + X$ signals with significance around 2σ. The results are translated into upper limits on $\sigma(gg \to R) \times \mathcal{B}(R \to SH \times \mathcal{B}(H \to ZZ) \times \mathcal{B}(ZZ \to 4\ell)$ and $\sigma(gg \to A) \times \mathcal{B}(A \to ZH) \times \mathcal{B}(H \to ZZ) \times \mathcal{B}(ZZZ \to 4\ell)$ at 95% confidence. For the $R \to SH \to 4\ell + E_{\mathrm{T}}^{\mathrm{miss}}$ signal, the observed (expected) upper limits range from 0.031–0.539 (0.034–0.343) fb for $(m_R, m_H) = (390, 220)$ GeV to $(m_R, m_H) = (1300, 1000)$ GeV. For the $A \to ZH \to 4\ell + X$ signal, the observed (expected) upper limits range from 0.027–0.419 (0.035–0.335) fb for $(m_A, m_H) = (320, 220)$ GeV to $(m_A, m_H) = (1300, 1000)$ GeV.

Acknowledgements

We thank CERN for the very successful operation of the LHC, as well as the support staff from our institutions without whom ATLAS could not be operated efficiently.

We acknowledge the support of ANPCyT, Argentina; YerPhI, Armenia; ARC, Australia; BMWFW and FWF, Austria; ANAS, Azerbaijan; CNPq and FAPESP, Brazil; NSERC, NRC and CFI, Canada; CERN; ANID, Chile; CAS, MOST and NSFC, China; Minciencias, Colombia; MEYS CR, Czech Republic; DNRF and DNSRC, Denmark; IN2P3-CNRS and CEA-DRF/IRFU, France; SRNSFG, Georgia; BMBF, HGF and MPG, Germany; GSRI, Greece; RGC and Hong Kong SAR, China; ISF and Benoziyo Center, Israel; INFN, Italy; MEXT and JSPS, Japan; CNRST, Morocco; NWO, Netherlands; RCN, Norway; MEiN, Poland; FCT, Portugal; MNE/IFA, Romania; MESTD, Serbia; MSSR, Slovakia; ARRS and MIZŠ, Slovenia; DSI/NRF, South Africa; MICINN, Spain; SRC and Wallenberg Foundation, Sweden; SERI, SNSF and Cantons of Bern and Geneva, Switzerland; MOST, Taiwan; TENMAK, Türkiye; STFC, United Kingdom; DOE and NSF, United States of America. In addition, individual groups and members have received support from BCKDF, CANARIE, Compute Canada and CRC, Canada; PRIMUS 21/SCI/017 and UNCE SCI/013, Czech Republic; COST, ERC, ERDF, Horizon 2020 and Marie Skłodowska-Curie Actions, European Union; Investissements d'Avenir Labex, Investissements d'Avenir Idex and ANR, France; DFG and AvH Foundation, Germany; Herakleitos, Thales and Aristeia programmes co-financed by EU-ESF and the Greek NSRF, Greece; BSF-NSF and MINERVA, Israel; Norwegian Financial Mechanism 2014-2021, Norway; NCN and NAWA, Poland; La Caixa Banking Foundation, CERCA Programme Generalitat de Catalunya and PROMETEO and GenT Programmes Generalitat Valenciana, Spain; Göran Gustafssons Stiftelse, Sweden; The Royal Society and Leverhulme Trust, United Kingdom.

The crucial computing support from all WLCG partners is acknowledged gratefully, in particular from CERN, the ATLAS Tier-1 facilities at TRIUMF (Canada), NDGF (Denmark, Norway, Sweden), CC-IN2P3 (France), KIT/GridKA (Germany), INFN-CNAF (Italy), NL-T1 (Netherlands), PIC (Spain), ASGC (Taiwan), RAL (UK) and BNL (USA), the Tier-2 facilities worldwide and large non-WLCG resource providers. Major contributors of computing resources are listed in Ref. [96].

Appendix

A Local p_0 values

The local p_0 value gauges the excess in the data, which is the probability of observing fluctuation above the background. Figure 8 shows the local p_0 values on the m_R–m_H and m_A–m_H planes for $R \to SH \to 4\ell + E_{\mathrm{T}}^{\mathrm{miss}}$ and $A \to ZH \to 4\ell + X$ processes, respectively. For the $R \to SH \to 4\ell + E_{\mathrm{T}}^{\mathrm{miss}}$ signal, the highest observed excess is around $m_H = 620$ GeV for $m_R \in [820, 1300]$ GeV with a local significance of up to 2.3σ. For the $A \to ZH \to 4\ell + X$, the highest excess for this signal is around $(m_H, m_A) = (380, 510)$ GeV with a local significance of 2.5σ.

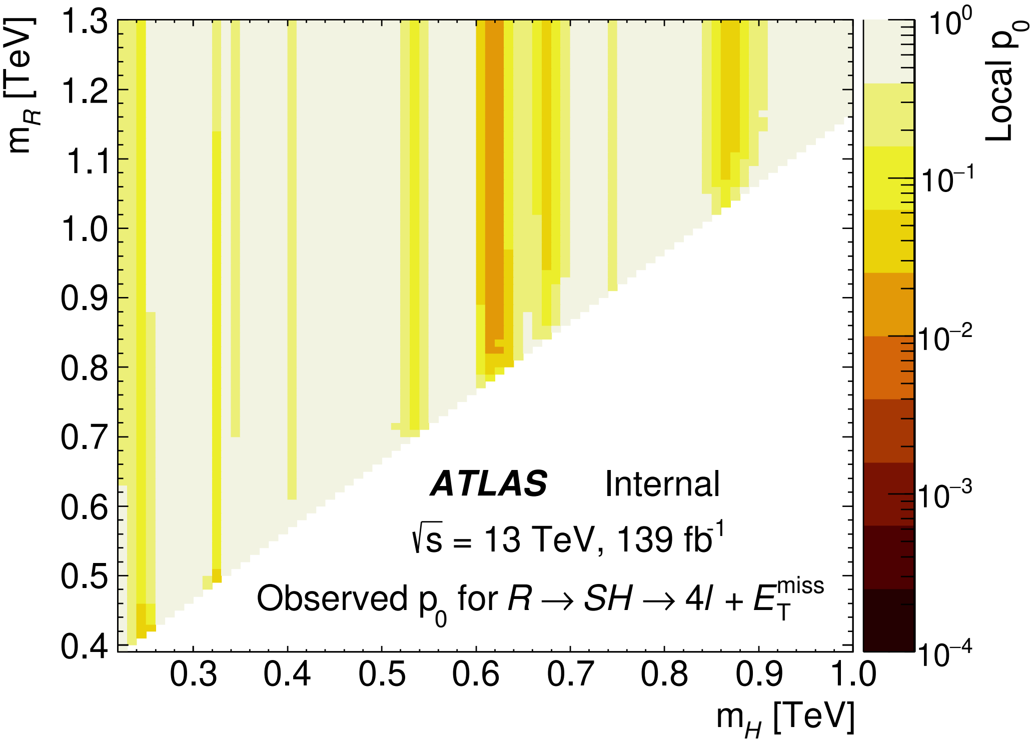

(a)

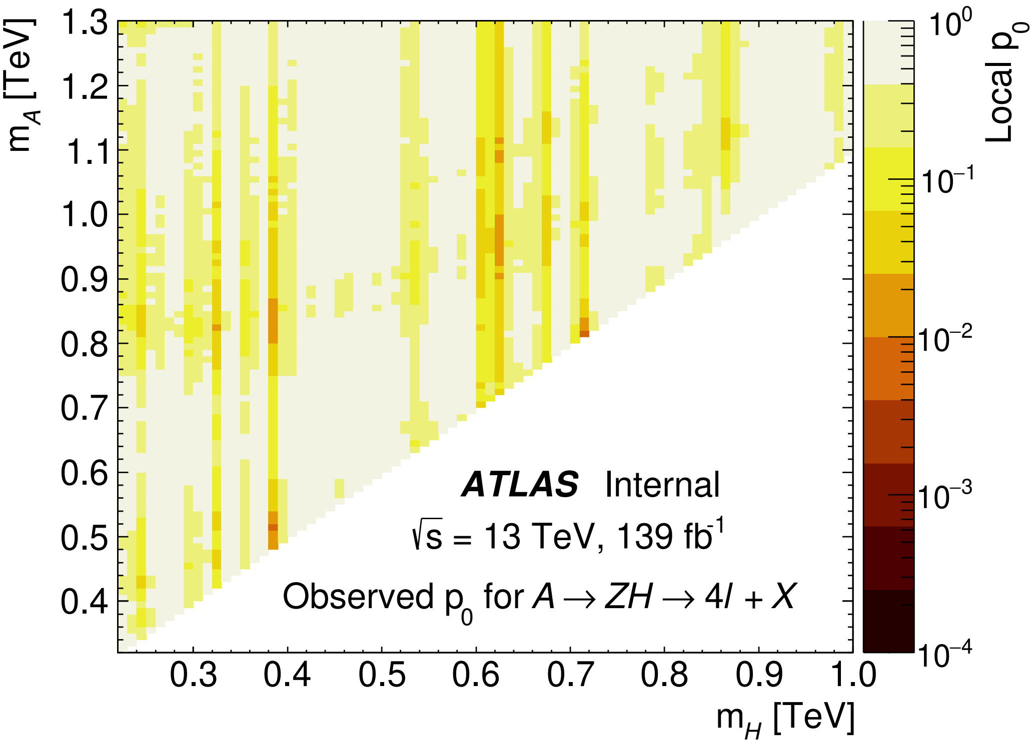

(b)

Figure 8: The local p_0 values on the two-dimensional contour of the (m_H, m_R) plane for (a) the $R \to SH \to 4\ell + E_{\mathrm{T}}^{\mathrm{miss}}$ signal with m_S = 160 GeV, and on the (m_H, m_A) plane for (b) the $A \to ZH \to 4\ell + X$ signal. The z-axis displays the local p_0 values.

References

[1] ATLAS Collaboration, *Observation of a new particle in the search for the Standard Model Higgs boson with the ATLAS detector at the LHC*, Phys. Lett. B **716** (2012) 1, arXiv: 1207.7214 [hep-ex] (cit. on p. 2).

[2] CMS Collaboration, *Observation of a new boson at a mass of 125 GeV with the CMS experiment at the LHC*, Phys. Lett. B **716** (2012) 30, arXiv: 1207.7235 [hep-ex] (cit. on p. 2).

[3] ATLAS Collaboration, *Measurements of the Higgs boson production and decay rates and coupling strengths using pp collision data at $\sqrt{s} = 7$ and 8 TeV in the ATLAS experiment*, Eur. Phys. J. C **76** (2016) 6, arXiv: 1507.04548 [hep-ex] (cit. on p. 2).

[4] ATLAS Collaboration, *Study of the spin and parity of the Higgs boson in diboson decays with the ATLAS detector*, Eur. Phys. J. C **75** (2015) 476, arXiv: 1506.05669 [hep-ex] (cit. on p. 2), Erratum: Eur. Phys. J. C **76** (2016) 152.

[5] CMS Collaboration, *Precise determination of the mass of the Higgs boson and tests of compatibility of its couplings with the standard model predictions using proton collisions at 7 and 8 TeV*, Eur. Phys. J. C **75** (2015) 212, arXiv: 1412.8662 [hep-ex] (cit. on p. 2).

[6] CMS Collaboration, *Constraints on the spin-parity and anomalous HVV couplings of the Higgs boson in proton collisions at 7 and 8 TeV*, Phys. Rev. D **92** (2015) 012004, arXiv: 1411.3441 [hep-ex] (cit. on p. 2).

[7] H. E. Haber and G. L. Kane, *The Search for Supersymmetry: Probing Physics Beyond the Standard Model*, Phys. Rept. **117** (1985) 75 (cit. on p. 2).

[8] N. Arkani-Hamed, S. Dimopoulos and G. R. Dvali, *The hierarchy problem and new dimensions at a millimeter*, Phys. Lett. B **429** (1998) 263, arXiv: hep-ph/9803315 (cit. on p. 2).

[9] G. F. Giudice, *Naturally Speaking: The Naturalness Criterion and Physics at the LHC*, 2008, arXiv: 0801.2562 [hep-ph] (cit. on p. 2).

[10] G. C. Branco et al., *Theory and phenomenology of two-Higgs-doublet models*, Phys. Rept. **516** (2012) 1, arXiv: 1106.0034 [hep-ph] (cit. on p. 2).

[11] T. D. Lee, *A Theory of Spontaneous T Violation*, Phys. Rev. D **8** (1973) 1226, ed. by G. Feinberg (cit. on p. 2).

[12] S. von Buddenbrock et al., *Phenomenological signatures of additional scalar bosons at the LHC*, Eur. Phys. J. C **76** (2016) 580, arXiv: 1606.01674 [hep-ph] (cit. on pp. 2, 3).

[13] M. Muhlleitner, M. O. P. Sampaio, R. Santos and J. Wittbrodt, *The N2HDM under Theoretical and Experimental Scrutiny*, JHEP **03** (2017) 094, arXiv: 1612.01309 [hep-ph] (cit. on p. 2).

[14] S. von Buddenbrock et al., *Multi-lepton signatures of additional scalar bosons beyond the Standard Model at the LHC*, J. Phys. G **45** (2018) 115003, arXiv: 1711.07874 [hep-ph] (cit. on p. 3).

[15] A. G. Cohen, D. B. Kaplan and A. E. Nelson, *Progress in electroweak baryogenesis*, Ann. Rev. Nucl. Part. Sci. **43** (1993) 27, arXiv: hep-ph/9302210 (cit. on p. 3).

[16] ATLAS Collaboration, *Combination of searches for Higgs boson pairs in pp collisions at $\sqrt{s}$ =13 TeV with the ATLAS detector*, Phys. Lett. B **800** (2020) 135103, arXiv: 1906.02025 [hep-ex] (cit. on p. 3).

[17] CMS Collaboration, *Combination of searches for Higgs boson pair production in proton-proton collisions at $\sqrt{s}$ = 13 TeV*, Phys. Rev. Lett. **122** (2019) 121803, arXiv: 1811.09689 [hep-ex] (cit. on p. 3).

[18] ATLAS Collaboration, *Searches for heavy ZZ and ZW resonances in the $\ell\ell qq$ and $\nu\nu qq$ final states in pp collisions at $\sqrt{s}$ = 13 TeV with the ATLAS detector*, JHEP **03** (2018) 009, arXiv: 1708.09638 [hep-ex] (cit. on p. 3).

[19] ATLAS Collaboration, *Search for WW/WZ resonance production in $\ell\nu qq$ final states in pp collisions at $\sqrt{s}$ = 13 TeV with the ATLAS detector*, JHEP **03** (2018) 042, arXiv: 1710.07235 [hep-ex] (cit. on p. 3).

[20] ATLAS Collaboration, *Search for heavy diboson resonances in semileptonic final states in pp collisions at $\sqrt{s}$ = 13 TeV with the ATLAS detector*, Eur. Phys. J. C **80** (2020) 1165, arXiv: 2004.14636 [hep-ex] (cit. on p. 3).

[21] ATLAS Collaboration, *Search for diboson resonances in hadronic final states in 139 fb^{-1} of pp collisions at $\sqrt{s}$ = 13 TeV with the ATLAS detector*, JHEP **09** (2019) 091, [Erratum: JHEP 06, 042 (2020)], arXiv: 1906.08589 [hep-ex] (cit. on p. 3).

[22] CMS Collaboration, *Search for a heavy Higgs boson decaying to a pair of W bosons in proton-proton collisions at $\sqrt{s}$ = 13 TeV*, JHEP **03** (2020) 034, arXiv: 1912.01594 [hep-ex] (cit. on p. 3).

[23] CMS Collaboration, *Search for a new scalar resonance decaying to a pair of Z bosons in proton-proton collisions at $\sqrt{s}$ = 13 TeV*, JHEP **06** (2018) 127, [Erratum: JHEP 03, 128 (2019)], arXiv: 1804.01939 [hep-ex] (cit. on p. 3).

[24] ATLAS Collaboration, *Search for heavy resonances decaying into a W or Z boson and a Higgs boson in final states with leptons and b-jets in 36 fb^{-1} of $\sqrt{s}$ = 13 TeV pp collisions with the ATLAS detector*, JHEP **03** (2018) 174, [Erratum: JHEP 11, 051 (2018)], arXiv: 1712.06518 [hep-ex] (cit. on p. 3).

[25] CMS Collaboration, *Search for a heavy pseudoscalar Higgs boson decaying into a 125 GeV Higgs boson and a Z boson in final states with two tau and two light leptons at $\sqrt{s}$ = 13 TeV*, JHEP **03** (2020) 065, arXiv: 1910.11634 [hep-ex] (cit. on p. 3).

[26] CMS Collaboration, *Search for neutral resonances decaying into a Z boson and a pair of b jets or τ leptons*, Phys. Lett. B **759** (2016) 369, arXiv: 1603.02991 [hep-ex] (cit. on p. 3).

[27] A. M. Sirunyan et al., *Search for new neutral Higgs bosons through the $H \rightarrow ZA \rightarrow \ell^+\ell^-\mathrm{b\bar{b}}$ process in pp collisions at $\sqrt{s}$ = 13 TeV*, JHEP **03** (2020) 055, arXiv: 1911.03781 [hep-ex] (cit. on p. 3).

[28] ATLAS Collaboration, *Search for a heavy Higgs boson decaying into a Z boson and another heavy Higgs boson in the $\ell\ell bb$ final state in pp collisions at $\sqrt{s}$ = 13 TeV with the ATLAS detector*, Phys. Lett. B **783** (2018) 392, arXiv: 1804.01126 [hep-ex] (cit. on p. 3).

[29] ATLAS Collaboration, *Search for a heavy Higgs boson decaying into a Z boson and another heavy Higgs boson in the $\ell\ell bb$ and $\ell\ell WW$ final states in pp collisions at $\sqrt{s} = 13$ TeV with the ATLAS detector*, Eur. Phys. J. C **81** (2021) 396, arXiv: 2011.05639 [hep-ex] (cit. on p. 3).

[30] ATLAS Collaboration, *The ATLAS Experiment at the CERN Large Hadron Collider*, JINST **3** (2008) S08003 (cit. on p. 4).

[31] ATLAS Collaboration, *Study of the mechanical stability of the ATLAS Insertable B-Layer*, ATL-INDET-PUB-2015-001, 2015, URL: https://cds.cern.ch/record/2022587 (cit. on p. 4).

[32] ATLAS Collaboration, *Performance of the ATLAS trigger system in 2015*, Eur. Phys. J. C **77** (2017) 317, arXiv: 1611.09661 [hep-ex] (cit. on p. 4).

[33] ATLAS Collaboration, *Operation and performance of the ATLAS semiconductor tracker*, JINST **9** (2014) P08009, arXiv: 1404.7473 [hep-ex] (cit. on p. 4).

[34] ATLAS Collaboration, *Monitoring and data quality assessment of the ATLAS liquid argon calorimeter*, JINST **9** (2014) P07024, arXiv: 1405.3768 [hep-ex] (cit. on p. 4).

[35] ATLAS Collaboration, *Selection of jets produced in* 13 *TeV proton–proton collisions with the ATLAS detector*, ATLAS-CONF-2015-029, 2015, URL: https://cds.cern.ch/record/2037702 (cit. on p. 4).

[36] ATLAS Collaboration, *The ATLAS Simulation Infrastructure*, Eur. Phys. J. C **70** (2010) 823, arXiv: 1005.4568 [physics.ins-det] (cit. on p. 4).

[37] S. Agostinelli et al., *GEANT4–a simulation toolkit*, Nucl. Instrum. Meth. A **506** (2003) 250 (cit. on p. 4).

[38] T. Sjöstrand, S. Mrenna and P. Z. Skands, *A Brief Introduction to PYTHIA 8.1*, Comput. Phys. Commun. **178** (2008) 852, arXiv: 0710.3820 [hep-ph] (cit. on p. 4).

[39] R. D. Ball et al., *Parton distributions with LHC data*, Nucl. Phys. B **867** (2013) 244, arXiv: 1207.1303 [hep-ph] (cit. on pp. 4, 5).

[40] ATLAS Collaboration, *The Pythia 8 A3 tune description of ATLAS minimum bias and inelastic measurements incorporating the Donnachie–Landshoff diffractive model*, ATL-PHYS-PUB-2016-017, 2016, URL: https://cds.cern.ch/record/2206965 (cit. on p. 4).

[41] E. Bothmann et al., *Event Generation with Sherpa 2.2*, SciPost Phys. **7** (2019) 034, arXiv: 1905.09127 [hep-ph] (cit. on p. 4).

[42] T. Gleisberg and S. Höche, *Comix, a new matrix element generator*, JHEP **12** (2008) 039, arXiv: 0808.3674 [hep-ph] (cit. on p. 5).

[43] S. Schumann and F. Krauss, *A Parton shower algorithm based on Catani-Seymour dipole factorisation*, JHEP **03** (2008) 038, arXiv: 0709.1027 [hep-ph] (cit. on p. 5).

[44] S. Höeche, F. Krauss, M. Schönherr and F. Siegert, *A critical appraisal of NLO+PS matching methods*, JHEP **09** (2012) 049, arXiv: 1111.1220 [hep-ph] (cit. on p. 5).

[45] S. Höche, F. Krauss, M. Schönherr and F. Siegert, *QCD matrix elements + parton showers: The NLO case*, JHEP **04** (2013) 027, arXiv: 1207.5030 [hep-ph] (cit. on p. 5).

[46] S. Höche, F. Krauss, S. Schumann and F. Siegert, *QCD matrix elements and truncated showers*, JHEP **05** (2009) 053, arXiv: 0903.1219 [hep-ph] (cit. on p. 5).

[47] F. Buccioni et al., *OpenLoops 2*, Eur. Phys. J. C **79** (2019) 866, arXiv: 1907.13071 [hep-ph] (cit. on p. 4).

[48] F. Cascioli, P. Maierhöfer and S. Pozzorini, *Scattering Amplitudes with Open Loops*, Phys. Rev. Lett. **108** (2012) 111601, arXiv: 1111.5206 [hep-ph] (cit. on p. 4).

[49] A. Denner, S. Dittmaier and L. Hofer, *Collier: a fortran-based Complex One-Loop LIbrary in Extended Regularizations*, Comput. Phys. Commun. **212** (2017) 220, arXiv: 1604.06792 [hep-ph] (cit. on p. 4).

[50] R. D. Ball et al., *Parton distributions for the LHC Run II*, JHEP **04** (2015) 040, arXiv: 1410.8849 [hep-ph] (cit. on p. 5).

[51] J. Alwall, M. Herquet, F. Maltoni, O. Mattelaer and T. Stelzer, *MadGraph 5 : Going Beyond*, JHEP **06** (2011) 128, arXiv: 1106.0522 [hep-ph] (cit. on p. 5).

[52] T. Sjöstrand et al., *An Introduction to PYTHIA 8.2*, Comput. Phys. Commun. **191** (2015) 159, arXiv: 1410.3012 [hep-ph] (cit. on p. 5).

[53] S. Alioli, P. Nason, C. Oleari and E. Re, *A general framework for implementing NLO calculations in shower Monte Carlo programs: the POWHEG BOX*, JHEP **06** (2010) 043, arXiv: 1002.2581 [hep-ph] (cit. on p. 5).

[54] P. Nason, *A new method for combining NLO QCD with shower Monte Carlo algorithms*, JHEP **11** (2004) 040, arXiv: hep-ph/0409146 (cit. on p. 5).

[55] S. Frixione, P. Nason and C. Oleari, *Matching NLO QCD computations with parton shower simulations: the POWHEG method*, JHEP **11** (2007) 070, arXiv: 0709.2092 [hep-ph] (cit. on p. 5).

[56] ATLAS Collaboration, *ATLAS Pythia 8 tunes to 7 TeV data*, ATL-PHYS-PUB-2014-021, 2014, URL: https://cds.cern.ch/record/1966419 (cit. on p. 5).

[57] D. J. Lange, *The EvtGen particle decay simulation package*, Nucl. Instrum. Meth. A **462** (2001) 152 (cit. on p. 5).

[58] P. Nason and G. Zanderighi, *W^+W^- , WZ and ZZ production in the POWHEG-BOX-V2*, Eur. Phys. J. C **74** (2014) 2702, arXiv: 1311.1365 [hep-ph] (cit. on p. 5).

[59] ATLAS Collaboration, *Measurement of the Z/γ^* boson transverse momentum distribution in pp collisions at $\sqrt{s} = 7$ TeV with the ATLAS detector*, JHEP **09** (2014) 145, arXiv: 1406.3660 [hep-ex] (cit. on p. 5).

[60] H.-L. Lai et al., *New parton distributions for collider physics*, Phys. Rev. D **82** (2010) 074024, arXiv: 1007.2241 [hep-ph] (cit. on p. 5).

[61] J. Pumplin et al., *New generation of parton distributions with uncertainties from global QCD analysis*, JHEP **07** (2002) 012, arXiv: hep-ph/0201195 (cit. on p. 5).

[62] C. Anastasiou, L. J. Dixon, K. Melnikov and F. Petriello, *High precision QCD at hadron colliders: Electroweak gauge boson rapidity distributions at NNLO*, Phys. Rev. D **69** (2004) 094008, arXiv: hep-ph/0312266 (cit. on p. 5).

[63] D. Berdine, N. Kauer and D. Rainwater, *Breakdown of the Narrow Width Approximation for New Physics*, Phys. Rev. Lett. **99** (2007) 111601, arXiv: hep-ph/0703058 (cit. on p. 5).

[64] R. D. Ball et al., *Impact of Heavy Quark Masses on Parton Distributions and LHC Phenomenology*, Nucl. Phys. B **849** (2011) 296, arXiv: 1101.1300 [hep-ph] (cit. on p. 5).

[65] ATLAS Collaboration, *Electron and photon performance measurements with the ATLAS detector using the 2015–2017 LHC proton-proton collision data*, JINST **14** (2019) P12006, arXiv: 1908.00005 [hep-ex] (cit. on p. 6).

[66] ATLAS Collaboration, *Improved electron reconstruction in ATLAS using the Gaussian Sum Filter-based model for bremsstrahlung*, ATLAS-CONF-2012-047, 2012, URL: https://cds.cern.ch/record/1449796 (cit. on p. 6).

[67] ATLAS Collaboration, *Electron reconstruction and identification in the ATLAS experiment using the 2015 and 2016 LHC proton-proton collision data at $\sqrt{s}$ = 13 TeV*, Eur. Phys. J. C **79** (2019) 639, arXiv: 1902.04655 [physics.ins-det] (cit. on pp. 6, 13).

[68] ATLAS Collaboration, *Muon reconstruction performance of the ATLAS detector in proton–proton collision data at $\sqrt{s}$ =13 TeV*, Eur. Phys. J. C **76** (2016) 292, arXiv: 1603.05598 [hep-ex] (cit. on pp. 6, 13).

[69] ATLAS Collaboration, *Jet reconstruction and performance using particle flow with the ATLAS Detector*, Eur. Phys. J. C **77** (2017) 466, arXiv: 1703.10485 [hep-ex] (cit. on p. 7).

[70] ATLAS Collaboration, *Topological cell clustering in the ATLAS calorimeters and its performance in LHC Run 1*, Eur. Phys. J. C **77** (2017) 490, arXiv: 1603.02934 [hep-ex].

[71] M. Cacciari, G. P. Salam and G. Soyez, *The anti-k_t jet clustering algorithm*, JHEP **04** (2008) 063, arXiv: 0802.1189 [hep-ph] (cit. on p. 7).

[72] ATLAS Collaboration, *Jet energy scale measurements and their systematic uncertainties in proton-proton collisions at $\sqrt{s}$ = 13 TeV with the ATLAS detector*, Phys. Rev. D **96** (2017) 072002, arXiv: 1703.09665 [hep-ex] (cit. on pp. 7, 13).

[73] ATLAS Collaboration, *Performance of pile-up mitigation techniques for jets in pp collisions at $\sqrt{s}$ = 8 TeV using the ATLAS detector*, Eur. Phys. J. C **76** (2016) 581, arXiv: 1510.03823 [hep-ex] (cit. on p. 7).

[74] ATLAS Collaboration, *Tagging and suppression of pileup jets with the ATLAS detector*, ATLAS-CONF-2014-018, 2014, URL: https://cds.cern.ch/record/1700870 (cit. on p. 7).

[75] ATLAS Collaboration, *ATLAS b-jet identification performance and efficiency measurement with $t\bar{t}$ events in pp collisions at $\sqrt{s}$ = 13 TeV*, Eur. Phys. J. C **79** (2019) 970, arXiv: 1907.05120 [hep-ex] (cit. on p. 7).

[76] ATLAS Collaboration, *Optimisation and performance studies of the ATLAS b-tagging algorithms for the 2017-18 LHC run*, ATL-PHYS-PUB-2017-013, 2017, URL: https://cds.cern.ch/record/2273281 (cit. on p. 7).

[77] The ATLAS Collaboration,
Recommendations of the Physics Objects and Analysis Harmonisation Study Groups 2014,
tech. rep. ATL-COM-PHYS-2014-451, CERN, 2014,
URL: https://cds.cern.ch/record/1700874 (cit. on p. 7).

[78] M. Aaboud et al., *Performance of missing transverse momentum reconstruction with the ATLAS detector using proton-proton collisions at $\sqrt{s}$ = 13 TeV*, Eur. Phys. J. C **78** (2018) 903, arXiv: 1802.08168 [hep-ex] (cit. on p. 7).

[79] ATLAS Collaboration,
E_T^{miss} performance in the ATLAS detector using 2015–2016 LHC pp collisions,
ATLAS-CONF-2018-023, 2018, URL: https://cds.cern.ch/record/2625233 (cit. on p. 7).

[80] ATLAS Collaboration, *2015 start-up trigger menu and initial performance assessment of the ATLAS trigger using Run-2 data*, ATL-DAQ-PUB-2016-001, 2016,
URL: https://cds.cern.ch/record/2136007 (cit. on p. 7).

[81] ATLAS Collaboration, *Trigger Menu in 2016*, ATL-DAQ-PUB-2017-001, 2017,
URL: https://cds.cern.ch/record/2242069 (cit. on p. 7).

[82] V. Kostyukhin, *VKalVrt - package for vertex reconstruction in ATLAS.*, (2003),
URL: https://cds.cern.ch/record/685551 (cit. on p. 6).

[83] ATLAS Collaboration, *Search for an additional, heavy Higgs boson in the $H \to ZZ$ decay channel at $\sqrt{s} = 8$ TeV in pp collision data with the ATLAS detector*, Eur. Phys. J. C **76** (2016) 45, arXiv: 1507.05930 [hep-ex] (cit. on p. 8).

[84] ATLAS Collaboration, *Search for heavy ZZ resonances in the $\ell^+\ell^-\ell^+\ell^-$ and $\ell^+\ell^-\nu\bar{\nu}$ final states using proton–proton collisions at $\sqrt{s} = 13$ TeV with the ATLAS detector*,
Eur. Phys. J. C **78** (2018) 293, arXiv: 1712.06386 [hep-ex] (cit. on p. 8).

[85] ATLAS Collaboration,
Search for heavy resonances decaying into a pair of Z bosons in the $\ell^+\ell^-\ell'^+\ell'^-$ and $\ell^+\ell^-\nu\bar{\nu}$ final states using 139 fb^{-1} of proton–proton collisions at $\sqrt{s} = 13$ TeV with the ATLAS detector,
Eur. Phys. J. C **81** (2021) 332, arXiv: 2009.14791 [hep-ex] (cit. on p. 8).

[86] A. L. Read, *Linear interpolation of histograms*, Nucl. Instrum. Meth. A **425** (1999) 357 (cit. on p. 10).

[87] ATLAS Collaboration,
Luminosity determination in pp collisions at $\sqrt{s} = 13$ TeV using the ATLAS detector at the LHC,
ATLAS-CONF-2019-021, 2019, URL: https://cds.cern.ch/record/2677054 (cit. on p. 13).

[88] W. Buttinger, *Using Event Weights to account for differences in Instantaneous Luminosity and Trigger Prescale in Monte Carlo and Data*, tech. rep. ATL-COM-SOFT-2015-119, CERN, 2015,
URL: https://cds.cern.ch/record/2014726 (cit. on p. 13).

[89] ATLAS Collaboration, *Performance of the missing transverse momentum triggers for the ATLAS detector during Run-2 data taking*, JHEP **08** (2020) 080, arXiv: 2005.09554 [hep-ex] (cit. on p. 13).

[90] A. Kalogeropoulos and J. Alwall,
The SysCalc code: A tool to derive theoretical systematic uncertainties, 2018,
arXiv: 1801.08401 [hep-ph] (cit. on p. 13).

[91] J. Butterworth et al., *PDF4LHC recommendations for LHC Run II*, J. Phys. G **43** (2016) 023001, arXiv: 1510.03865 [hep-ph] (cit. on p. 13).

[92] J. Bellm et al., *Herwig 7.0/Herwig++ 3.0 release note*, Eur. Phys. J. C **76** (2016) 196, arXiv: 1512.01178 [hep-ph] (cit. on p. 13).

[93] G. Cowan, K. Cranmer, E. Gross and O. Vitells, *Asymptotic formulae for likelihood-based tests of new physics*, Eur. Phys. J. C **71** (2011) 1554, arXiv: 1007.1727 [physics.data-an] (cit. on pp. 14, 16), Erratum: Eur. Phys. J. C **73** (2013) 2501.

[94] ATLAS Collaboration, *Formulae for Estimating Significance*, All figures including auxiliary figures are available at https://atlas.web.cern.ch/Atlas/GROUPS/PHYSICS/PUBNOTES/ATL-PHYS-PUB-2020-025, 2020, URL: https://cds.cern.ch/record/2736148 (cit. on pp. 17–19).

[95] A. L. Read, *Presentation of search results: the CL_S technique*, J. Phys. G **28** (2002) 2693 (cit. on p. 16).

[96] ATLAS Collaboration, *ATLAS Computing Acknowledgements*, ATL-SOFT-PUB-2021-003, 2021, URL: https://cds.cern.ch/record/2776662 (cit. on p. 22).